Validation of the Aura MLS cloud ice water content measurements

Dong L. Wu,[1] Jonathan H. Jiang,[1] William G. Read,[1] Richard T. Austin,[2] Cory P. Davis,[3] Alyn Lambert,[1] Graeme L. Stephens,[2] Deborah G. Vane,[1] and Joe W. Waters[1]

[1] Retrieval and validation of upper tropospheric ice water content (IWC) measurements with the Aura Microwave Limb Sounder (MLS) are described. The MLS version 2.2 (V2.2) IWC, derived from 240-GHz cloud-induced radiances (*Tcir*) at high tangent heights, is scientifically useful at 215–83 hPa. The V2.2 IWC represents a bulk cloud property averaged over a $\sim$300 $\times$ 7 $\times$ 4 km^3 volume near the pointing tangent height. Precision, accuracy, and spatial resolution of the V2.2 IWC are determined through model simulations and comparisons with CloudSat observations. Comparisons of MLS V2.2 and CloudSat R03 IWCs are made for the months of January and July in terms of normalized probability density function (PDF). The differences between MLS and CloudSat IWC PDFs are generally less than 50% over the IWC range where the MLS technique is valid. At pressures <177 hPa and extratropical latitudes, the MLS V2.2 IWC exhibits a slightly low bias compared to CloudSat, part of which can be attributed to systematic errors in the MLS retrieval. Cloud inhomogeneity and particle size distribution are the leading sources of uncertainties in the V2.2 IWC.

Citation: Wu, D. L., J. H. Jiang, W. G. Read, R. T. Austin, C. P. Davis, A. Lambert, G. L. Stephens, D. G. Vane, and J. W. Waters (2008), Validation of the Aura MLS cloud ice water content measurements, *J. Geophys. Res.*, *113*, D15S10, doi:10.1029/2007JD008931.

1. Introduction

[2] Clouds are a major source of uncertainty in understanding and predicting climate variability [e.g., *Houghton et al.*, 2001]. Reducing the cloud uncertainty requires more observations than just cloud fraction and cloud top height that have been obtained to date from space. Global observations of ice water content (IWC), a key parameter for characterizing cloud radiative and hydrological properties, remain lacking, hampered in part by complicated microphysics in ice clouds [e.g., *Comstock et al.*, 2007]. Lack of observational guidance in climate models has led to poor-fidelity predictions about cloud feedbacks in a changing climate.

[3] Remote sensing of cloud ice with passive mm and sub-mm wave radiometry offers great potential for obtaining global cloud ice amount needed by climate and weather research. Recently, several studies have been made using microwave sensors to retrieve cloud ice water path (IWP) [e.g., *Vivekanandan et al.*, 1991; *Gasiewski*, 1992; *Evans and Stephens*, 1995; *Evans et al.*, 1998; *Liu and Curry*, 2000; *Weng and Grody*, 2000; *Skofronick-Jackson and Wang*, 2000; *Eriksson et al.*, 2007]. Unlike visible/IR techniques, microwave radiation can penetrate into dense clouds and interact with ice particles to make estimates of ice mass and other bulk properties like IWC and effective radius of ice crystals [*Evans et al.*, 2005].

[4] As a relatively new remote sensing technique, MLS (Microwave Limb Sounder) can measure cloud ice in the upper troposphere with millimeter and submillimeter wave limb radiometry [*Waters*, 1993; *Wu and Jiang*, 2004; *Wu et al.*, 2005; *Waters et al.*, 2006]. In addition to the advantages associated with nadir-viewing microwave sensors, the MLS technique does not require knowledge of atmospheric temperature lapse rate (as in the nadir case) for cloud detection and is not significantly affected by surface properties. In a previous study, *Wu et al.* [2005] made the first global IWC observations near the tropopause using the 203 GHz measurements acquired by UARS (Upper Atmosphere Research Satellite) MLS during 1991–1997. The UARS MLS study demonstrated that cloud features observed by microwaves can provide quantitative information on cloud ice amount in the upper troposphere, which has important implications for H$_2$O transport and dehydration in that region.

[5] Aura MLS was launched in July 2004 and has seven radiometers with frequencies near 118 (H,V), 190(V), 240(H), 640(H) GHz and 2.5 (H,V) THz for horizontal (H) and vertical (V) polarizations. All the MLS radiometers can detect cloud-induced radiance changes [*Wu et al.*, 2006]. Since the initial release of version 1.5 (V1.5) products in 2004, the MLS team made further improvements and released version 2.2 (V2.2) products in 2006. Both V1.5 and V2.2 IWC retrievals use 240 GHz measurements at

---
[1]Jet Propulsion Laboratory, California Institute of Technology, Pasadena, California, USA.
[2]Department of Atmospheric Science, Colorado State University, Fort Collins, Colorado, USA.
[3]Meteorological Service of New Zealand Limited, Wellington, New Zealand.

upper tropospheric tangent heights where the radiances penetrate through limb with contribution function peaking sharply at the tangent height.

[6] Initial analyses have showed the scientific value of this new global cloud ice data set. One of the poorly constrained problems in global climate models is cloud parameterization. Some serious shortfalls in the models were uncovered as a result of comparisons between MLS and model cloud ice [*J.-L. Li et al.*, 2005; *Li et al.*, 2007]. The MLS cloud data were also used to study tropical super greenhouse effects [*Su et al.*, 2006] and roles of convective lifting in pollution transport [*Q. B. Li et al.*, 2005; *Fu et al.*, 2006]. In addition to upper tropospheric cloud ice, Aura MLS also measures temperature (T), H_2O, CO, O_3, and HNO_3 profiles [*Schwartz et al.*, 2008; *Read et al.*, 2007; *Livesey et al.*, 2008; *Jiang et al.*, 2007; *Santee et al.*, 2007], collectively providing a comprehensive view of deep convection, hydrological cycle, and transport in the upper troposphere. Aura is one of the NASA A-Train spacecrafts, flying in formation with Aqua, CloudSat and CALIPSO (Cloud-Aerosol Lidar and Infrared Pathfinder Satellite Observation). The A-Train sensors have collected large ensembles of closely sampled cloud data, and give an unprecedented opportunity for understanding and improving accuracy of global cloud ice measurements.

[7] The aim of this paper is to assess accuracy, precision, and resolution of the Aura MLS V2.2 IWC measurement through model simulations and comparisons with CloudSat. A better understanding of the IWC accuracy associated with passive microwave techniques like MLS is important for effectively and efficiently planning future global cloud ice remote sensing. Although active systems can provide IWC profiles with high horizontal and vertical resolution from space, mapping three-dimensional fast cloud processes will likely depend on passive remote-sensing systems. The validation of MLS 240-GHz IWC in this paper is a first step toward such a better understanding. In subsequent studies we plan to extend our investigation to MLS 640-GHz measurements, which have a better sensitivity to cloud ice from small particles.

2. Aura MLS IWC Measurements

### 2.1. Limb Radiances and Cloud Handling

[8] The Aura satellite has a 705-km sun-synchronous (~1:40 P.M. ascending crossing time) orbit with 98° inclination. MLS limb scans are synchronized to the orbital period with 240 limb scans (called the major frames or MAFs) per orbit in nominal operation. MLS latitude coverage is from 82°S to 82°N with the tangent track close to the Aqua nadir footprint but ~8 min behind. Unlike the step-and-stare scans used by UARS MLS, Aura MLS scans are continuous in tangent height (h_t) from the surface to ~92 km in 24.7s (which includes time for antenna retracing and radiometric calibration). The integration time for each measurement is 1/6 s, called a minor frame (MIF). For the GHz measurements, each MAF or scan has 40–50 MIFs that are useful for tropospheric cloud observations. These MIFs are separated by ~300 m in tangent height. More on the MLS operation, calibration, and noise characteristics can be found in the work by *Jarnot et al.* [2006].

[9] Except for the 118 GHz, all MLS radiometers are double-sideband receivers, meaning that the measured radiance is a sum of radiation from two frequency sidebands (separated by 4–40 GHz). Since the Aura MLS antenna views forward in the satellite flying direction, all scans are roughly within the same orbital plane and two scan profiles are separated by ~165 km along track. The MLS cross-track FOV (field-of-view) widths are 12, 8.4, 6.4, 2.9, and 2.1 km at 118, 190, 240, 640 GHz and 2.5 THz, respectively, whereas the corresponding vertical FOV widths are 5.8, 4.2, 3.2, 1.4, and 2.1 km [*Cofield and Stek*, 2006; *Pickett*, 2006].

[10] MLS cloud flags and cloud ice retrievals are made from radiance measurements in a window channel of each radiometer, but only the 240-GHz measurements are used for producing the standard IWC in V1.5 and V2.2. Compared to other channels, the window channels are least affected by clear-sky atmospheric absorption and can penetrate to a lower altitude with a better sensitivity to cloud effects. MLS radiances can be affected by clouds when the pointing tangent height is near or below cloud top. The fundamental quantity for MLS cloud measurements is the cloud-induced radiance (*Tcir*), which is defined as the difference between the measured radiance and the expected clear-sky radiances at each tangent pressure (*Ptan*). In the MLS V2.2 algorithm, the expected clear-sky radiance is calculated using the same radiative transfer (RT) model as in the Level 2 retrieval [*Read et al.*, 2006], which takes the retrieved atmospheric state as the model input.

[11] Clouds can induce both positive and negative *Tcir* in limb radiances depending on the background and scattering properties of ice particles in the path. *Tcir* is generally spectrally flat within a MLS radiometer bandwidth (a few GHz). However, where cloud scattering is strong, MLS radiance spectra may be altered considerably to induce a frequency-dependent *Tcir* even over a narrow spectral band. Such a spectrally dependent *Tcir* can be readily seen around strong gas emission lines by O_2, H_2O, and O_3 where cloud scattering has significantly redistributed the radiation. As a result, the observed radiance spectra are distorted from the clear-sky case and can cause artifacts in MLS gas retrievals. Therefore, the radiances from these strong cloud scattering cases need to be excluded in the retrieval processing [*Read et al.*, 2006]. For those cases with small *Tcir*, the V2.2 algorithm can handle cloud effects by retrieving a radiance-additive baseline or extinction profile.

[12] As in MLS V1.5 data processing [*Livesey et al.*, 2006], the V2.2 algorithm retrieves atmospheric gas profiles and *Tcir* iteratively (Appendix A). In MLS Level 2 data processing, *Tcir* is used to flag the radiance measurements that are possibly contaminated by clouds. A cloudy case is where *Tcir* is significantly above or below the uncertainty expected for the modeled clear-sky radiance. The quality of derived *Tcir* improves as the retrieval progresses, but we set a fixed upper and a lower bound to flag *Tcir* outliers and a flag is generated separately for each radiometer at each MIF with *Ptan* > 46 hPa (Appendix A). The *Tcir* in these intermediate steps are not used for cloud ice retrieval. Instead, they provide initial indication on cloud presence at each limb position for improving the clear-sky gas retrievals. The quality of clear-sky gas retrievals determines the quality of the final *Tcir* that will be used for the cloud ice
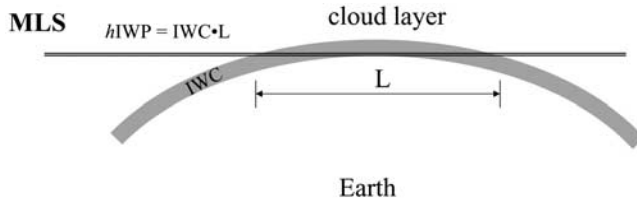
Figure 1. Schematic diagram to illustrate the radiative transfer of MLS radiance through an atmosphere with a single cloud layer. *Tcir* is proportional to horizontal ice water path (*h*IWP). Knowing the characteristic cloud length, **L**, we may relate *Tcir* directly to IWC of the cloud layer near the tangent height (see text).

retrieval. *Tcir* is usually computed at the end of a retrieval phase in preparation for the next retrieval phase. As an exception, the R3 (240 GHz) cloud flag is based on the chi-square (χ^2) value of band 8 radiances (233.9 GHz $^{16}O^{18}O$ line), which is based on the radiance fit of the entire band 8 at the end of the *Core* phase (Appendix A). The *Tcir* calculation is finalized in the *HighCloud* phase for all MLS radiometers (see Appendix A) after the key atmospheric profiles (*T*, *Ptan*, H_2O, O_3, HNO_3) are retrieved. The IWC retrieval is based on the final 240-GHz *Tcir* result and is derived as follows. The radiative transfer (RT) model computes the expected clear-sky radiances using the best atmospheric state retrieved before *HighCloud* phase. In addition, the retrieved H_2O is capped such as the corresponding relative humidity with respect to ice (*RHi*) does not exceed 110%. This constraint helps to eliminate *Tcir* spikes occasionally generated from the H_2O retrieval, but it may induce extra error from the *T* retrieval. The difference between the measured and the modeled radiances gives the final *Tcir*. The *Tcir*'s derived from each retrieval phase are stored in the Level 2 auxiliary file (L2AUX-Cloud) for further diagnoses.

2.2. Cloudy-Sky Radiative Transfer Models

2.2.1. One-Dimensional Model

[13] For MLS IWC retrieval, we developed a 1-D RT model to compute MLS-like limb radiances under a cloudy but spherically stratified atmosphere [*Wu et al.*, 2006]. In the 1-D model all atmospheric and cloud variables vary only vertically. The model assumes spherical ice particles in cloud layers, and cloud volume absorption/scattering coefficients and phase functions are obtained from the Mie solution. Multiple scattering effects are included through an iterative approach of solving the RT equation [*Wilheit et al.*, 1982; *Yeh et al.*, 1990] but polarization effects are neglected. Cloud particle size distributions (PSDs) are based on the parameterization developed by *McFarquhar and Heymsfield* [1997] (hereinafter referred to as MH97). Finally, the 1-D radiance model approximates the MLS sideband (232.5 and 246.9 GHz) mixing with a 50% sideband ratio and neglects FOV effects.

[14] A model atmosphere (Figure 1) is used for obtaining MLS cloud retrieval coefficients. It contains a single 2-km thick cloud layer centered at altitude h_0 with a trapezoid vertical distribution that is uniform in the center 1 km and linearly decays in the top and bottom half km (Appendix B).

To obtain *Tcir* dependence on IWC, we change cloud ice amount by multiplying this cloud profile with different IWC values. In essence, MLS *Tcir* is a direct measure of horizontal ice water path (*h*IWP), a column of cloud ice along the line of sight (LOS). The *h*IWP at $h_t = h_0$ can be converted to an IWC as an estimate of cloud ice in the cloud layer using an equivalent horizontal length **L**. In this case (Figure 1 and Appendix B), **L** is ~200 km. The background clear-sky atmosphere is based on the tropical temperature profile from the CIRA (COSPAR International Reference Atmosphere) reference atmosphere for January [*Fleming et al.*, 1988]. In addition, the model assumes 100% in-cloud *RHi* but 50% elsewhere at pressures > 100 hPa. Above that pressure level, *RHi* is relaxed to the value of a typical stratospheric profile. The model also includes O_3 because of its significant contributions in the 240 GHz channel, which along with the model *T* and *RHi* profiles are given in Figure 2.

[15] Figure 3 shows the calculated *Tcir* profiles (averaged for the 232.5 and 246.9 GHz sidebands) from the atmosphere with the 2-km cloud layer centered at 16 km altitude. As seen in Figure 3a, the cloud layer can greatly alter the radiance profiles by increasing (decreasing) brightness temperature at tangent heights above (below) ~9 km where the background radiances are relatively low (high). The *Tcir* increase with respect to *h*IWP is nearly linear at small values but becomes saturated at *h*IWP ~ 15 kg/m^2 or IWC ~ 100 mg/m^3 as the cloud is opaque.

[16] Figure 3b shows that the slope of the linear portion of the calculated *Tcir*-*h*IWP relation is nearly constant for all the tangent heights. After converting *Tcir* to the mean IWC of the cloud layer (Appendix B), we have *Tcir*(h_t) $\propto$ IWC($h_0 = h_t$), which is essentially the modeled *Tcir*-IWC relation in Figure 3c. To obtain the *Tcir*-IWC relation at a different tangent height, we place the cloud layer at that tangent height and repeat the same calculations as for the h_t = 16 km case. In V2.2 IWC retrieval we fit the modeled *Tcir*-IWC relation with

$$Tcir = Tcir_0\left(1 - e^{IWC/IWC_0}\right) \tag{1}$$
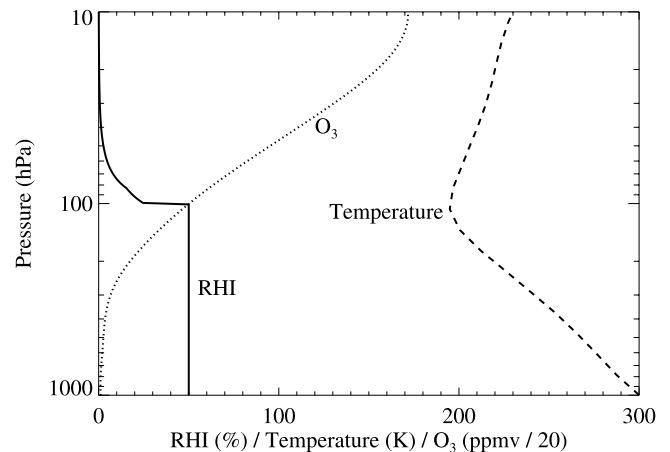
Figure 2. The temperature, *RHi* and O_3 profiles used for modeling MLS *Tcir*-IWC relations. The O_3 profile is in ppmv but multiplied by 20 on this scale.
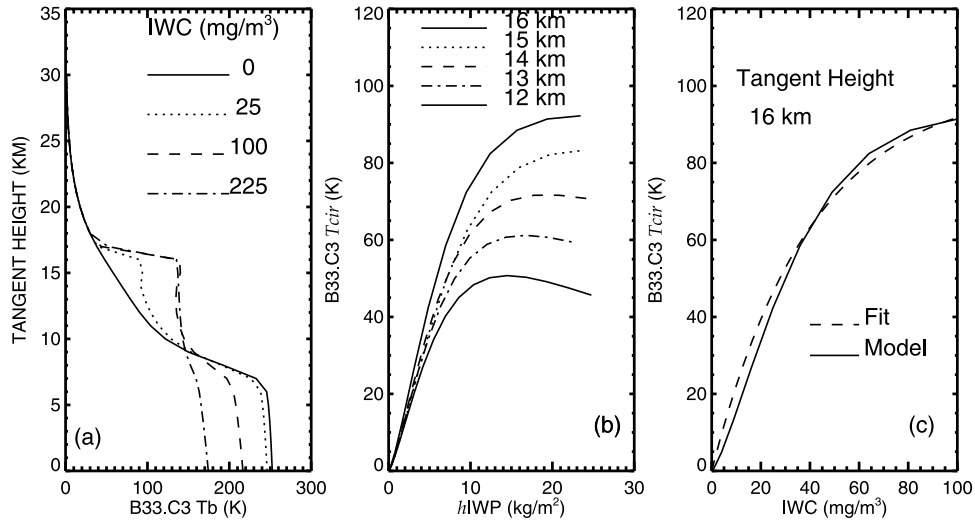
Figure 3. (a) Modeled limb radiances of the MLS 240-GHz window channel (averaged for the 232.5 and 246.9 GHz sidebands). A 2-km cloud layer is placed at 16 km with a trapezoid distribution (see Appendix B). (b) *Tcir*-*h*IWP relations for the 240-GHz window channel at different tangent heights. (c) Modeled (solid line) and fitted (dashed line) *Tcir*-IWC relation at h_t = 16 km for the 240-GHz channel.

where the fitting parameters $Tcir_0$ and IWC_0 are given in Table 1. Equation (1) assumes the instrument vertical FOV is infinitely sharp. As seen in Table 1, parameters $Tcir_0$ and IWC_0 vary slightly with tangent height. One may modify the coefficients in Table 1 by averaging the values vertically to account a finite instrument FOV, but the resulting differences are relatively small.

[17] The *Tcir*-IWC relations are similar to those of the 2-km layer case if IWC has an extensive vertical distribution and decreases exponentially with height, or $IWC \propto e^{-z/H_0}$, where H_0 is the mean scale height of IWC profiles. Such an exponential vertical distribution is consistent with the climatology from in situ observations in the upper troposphere [*Heymsfield and Donner*, 1990; *McFarquhar and Heymsfield*, 1996], and H_0 was found to be ∼2 km in the tropical upper troposphere but ∼1 km near the tropopause. Assuming $IWC \propto e^{-z/H_0}$, we find that *Tcir* is still proportional to the IWC at pointing tangent height except that the characteristic length $L \approx 200\sqrt{H_0}$. (Appendix B). Hence, equation (1) is generalized to approximate all upper tropospheric clouds, and the characteristic horizontal length **L** used to convert the *Tcir*-*h*IWP relation to the *Tcir*-IWC relation is 200–300 km.

2.2.2. Two-Dimensional Model

[18] To better understand cloud inhomogeneity effects on MLS IWC retrieval and spatial resolution, we developed a 2-D cloudy-sky RT model, based on the 2-D clear-sky model in which MLS FOV effects are included and along-track inhomogeneity is better resolved [*Read et al.*, 2006]. We modified the 2-D clear-sky model to include contributions from cloud emission and scattering volume coefficients, as expressed by *Wu et al.* [2006, equation (3)]. The same assumptions and approximations are applied to cloud scattering calculations as in the 1-D model, but with single scattering. For the clouds within the linear regime in Figure 3, we find with in the 1-D RT model, which takes into account multiple scattering through an iterative approach of solving the RT equation, that the cloudy-sky radiance solution

generally converges within one iteration. In other words, light is scattered once in the cloudy-sky radiance calculations. Thus, for these clouds multiple scattering effects can be neglected. This 2-D cloudy-sky model is employed later to simulate the V2.2 *Tcir* for various broken cloud conditions.

[19] Through the Taylor expansion, IWC-induced *Tcir* is linearized about the mean state $Tcir_0$ to yield a linearized 2-D model, mathematically, written as

$$Tcir(P_{tam}, IWC) = Tcir_0(P_{tam}, IWC_0)$$
$$+ \sum_{i,k} WF(x_i, z_k, P_{tan}, IWC_0)(IWC - IWC_0)$$

(2)

where i and k denote model horizontal and vertical indices, for x and z, respectively. $WF(x_i, z_k, P_{tan}, IWC_0)$ is the first derivative of *Tcir* with respect to IWC linearized at IWC_0, also called the IWC weighting function (WF), which is given by

$$WF(x_i, z_k, P_{tan}, IWC_0)$$
$$= \left.\frac{\partial T_{ik}cir}{\partial IWC}\right|_{IWC=IWC_0}$$
$$= \left.\left(\frac{\partial T_{ik}cir}{\partial \beta_{ca}} \bullet \frac{\partial \beta_{ca}}{\partial IWC} + \frac{\partial T_{ik}cir}{\partial \beta_{cs}} \bullet \frac{\partial \beta_{cs}}{\partial IWC}\right)\right|_{IWC=IWC_0}$$

(3)

Table 1. Model Coefficients for the V2.2 *Tcir*-IWC Relation

P_{tan}, hPa	*Tcir* Bias,[a] K	$Tcir_0$, K	IWC_0, mg/m³
83	−1.5	100	40
100	−2.2	100	40
121	−2.5	100	43
147	−3.2	90	55
177	−4.2	80	69
215	−6.0	70	70
261	−7.5	50	50

[a]The *Tcir* bias is estimated from the real data, and interpolated to these fixed tangent pressures. Cause(s) of the *Tcir* bias will be discussed later in section 3.1 on systematic uncertainty.

where $T_{ik}cir$ is the component of $Tcir$ at location (x_i, z_k) and $Tcir = \Sigma_{i,k}T_{ik}cir$. The $T_{ik}cir$ derivatives with respect to cloud volume absorption (β_{ca}) and scattering (β_{cs}) coefficients, $\partial T_{ik}cir/\partial\beta_{ca}$ and $\partial T_{ik}cir/\partial\beta_{cs}$, are computed analytically using the formula developed for clear-sky volume absorption coefficients (*Read et al.*, 2006). The derivatives $\partial\beta_{ca}/\partial IWC$ and $\partial\beta_{cs}/\partial IWC$ are obtained from the Mie solution and the MH97 PSD as described by *Wu and Jiang* [2004]. Compared to the 1-D model, the 2-D RT model is more realistic because it accounts for vertical and along-track cloud inhomogeneity and includes the instrument FOV effects. Later in this paper, the 2-D model is used to assess instrument spatial resolution, 1-D model error, and cloud inhomogeneity effects on the V2.2 IWC retrieval.

[20] The 2-D RT model, however, is computationally intensive in computer time and memory. With limited computing resources, for the 2-D simulations we choose $0.5°$ ($\sim$50 km) along-track and 24 levels per decade ($\sim$0.67 km) vertical resolution as the model input for IWC profiles, and the background clear-sky atmosphere (Figure 2) is same as in the 1-D calculations.

2.3. Spatial Resolution

[21] To quantify spatial resolution of the V2.2 IWC measurements, we restrict our study to the optically thin situations at 215–83 hPa (that are used for the retrievals) where limb radiances are neither saturated by clouds nor by clear-sky gases. In these cases, as shown in Figure 4, the WFs from the linearized 2-D model (equation (3)) are mostly positive, which extend horizontally over a 200–400 km along track and more than 3 km vertically because of the instrument FOV and the spherical geometry. In this calculation, we assume a 10 mg/m^3 IWC uniformly distributed at pressures > 83 hPa and force the IWC profile to drop sharply (with a scale height of 0.5 km) above 83 hPa since clouds rarely reach altitudes above 18 km. The 10 mg/m^3 value is arbitrarily chosen to represent an optically thin cloud field. As long as the $Tcir$-IWC relation remains in the linear regime (IWC < $\sim$50 mg/m^3), the WF morphology at 215–83 hPa does not vary significantly.

[22] Although the WFs from a uniform 10 mg/m^3 at 215–83 hPa extend relatively widely and deeply to high altitudes, only the altitudes near the tangent height are most significant because climatologically $IWC \propto e^{-z/H_0}$. In reality, each MLS IWC represents an average of an ensemble of clouds within the WF, of which the IWC statistics can be characterized by the exponential distribution. This consideration allows us to approximate the calculated WF with a rectangular box as shown in Figure 4 and ignore the contributions from upper left and right corners. As long as the $IWC \propto e^{-z/H_0}$ distribution holds, $Tcir$ will be contributed mostly from IWC in the volume near the pointing tangent height. The horizontal and vertical resolutions of these rectangular boxes are approximately given by $200\sqrt{H_0}$ and $3.2 + 1.8/H_0$, respectively (Appendix B). According to in situ observations, IWC profiles tend to have $H_0 = \sim$1 km above $\sim$14 km and $H_0 = \sim$2 km below that height.

[23] To evaluate validity of the rectangular box approximation, we use 50-km averaged CloudSat IWC profiles as the input to the model WFs in Figure 4, and compare the fully integrated $Tcir$ (by convolving the 2-D WFs with CloudSat IWC profiles) with boxcar-averaged $Tcir$. We refine the horizontal and vertical dimensions of the rectangular box to best fit the fully integrated $Tcir$ (Figure 5). The final horizontal and vertical dimensions of the rectangular boxes are plotted in Figure 4 for each pressure level. The fully integrated and box-averaged $Tcir$'s correlate well with each other (Figure 5), showing overall good 1:1 correlation for a large dynamic range. At 215–147 hPa, there are relatively small (<20%) biases introduced because of the boxcar approximation. The bias increases to $\sim$50% at 121 hPa, 50–100% at 100 hPa and $\sim$100% at 83 hPa, showing systematically smaller values from the box-averaged $Tcir$, which mean that the V2.2 IWC is likely biased high as the box mean. The overall agreement suggests that the rectangular box is a good approximation to the WFs in Figure 4 at pressures 215–83 hPa. In addition, the derived box dimensions are consistent with the values estimated from $IWC \propto e^{-z/H_0}$ distributions, yielding the (horizontal, vertical) resolutions of (300, 4), (250, 4), and (200, 5) km at 215–147, 121, 100–83 hPa, respectively.

[24] Figure 4 also reveals some limitations of the simple IWC retrieval technique used in the V2.2 algorithm. The V2.2 IWC retrieval assumes that $Tcir$ increase monotonically with IWC, which is only valid at tangent pressures <261 hPa where the 2-D WFs are dominated by positive contributions. At 261 hPa and below, negative weights begin to make a significant contribution to $Tcir$, offsetting effects by the positive weights and causing reduced $Tcir$ sensitivity to IWC. Depending on the amount of cloud ice in the path, the 240-GHz radiance generally has a poor sensitivity to cloud ice at these transition tangent pressures (383–261 hPa) [*Wu and Jiang*, 2004]. At tangent pressures > 383 hPa, the WFs are dominated by negative contributions because clouds tend to scatter upwelling radiation out of the MLS LOS, reducing brightness temperature in limb radiance. The negative $Tcir$ at these tangent heights can be used to retrieve a cloud ice column (above $\sim$6 km), which is beyond the scope of the paper and will be discussed in a future study.

2.4. V2.2 IWC Retrieval

[25] The V2.2 algorithm retrieves IWC from the 240-GHz $Tcir$ at pressures $\leq$215 hPa by converting $Tcir$ directly to IWC. As a volume-averaged quantity over the aforementioned equivalent *L* along the LOS, the 2-D dimensions of V2.2 IWC are characterized by the rectangular boxes in Figure 4. The retrieval uses the $Tcir$-IWC relation in equation (1) where the parameters ($Tcir_0$, IWC$_0$) are given in Table 1.

[26] As discussed later in section 3.1, the 240-GHz $Tcir$ derived from the measured and modeled radiances contains a bias that varies with pressure and latitude. Prior to the V2.2 IWC retrieval, an estimated $Tcir$ bias with fixed values for all latitudes (Table 1) is removed. The corrected $Tcir$ are then averaged onto the standard MLS horizontal (1.5° along track) and vertical (12 levels per decade) grids before converted to IWC using the modeled $Tcir$-IWC relations (equation (1)). Since each MLS scan is closely associated with a retrieval grid box, the binning does not significantly degrade the horizontal resolution of MLS IWC. MLS scans provide very dense (every $\sim$300 m) vertical sampling in the upper troposphere and lower stratosphere (UT/LS), and
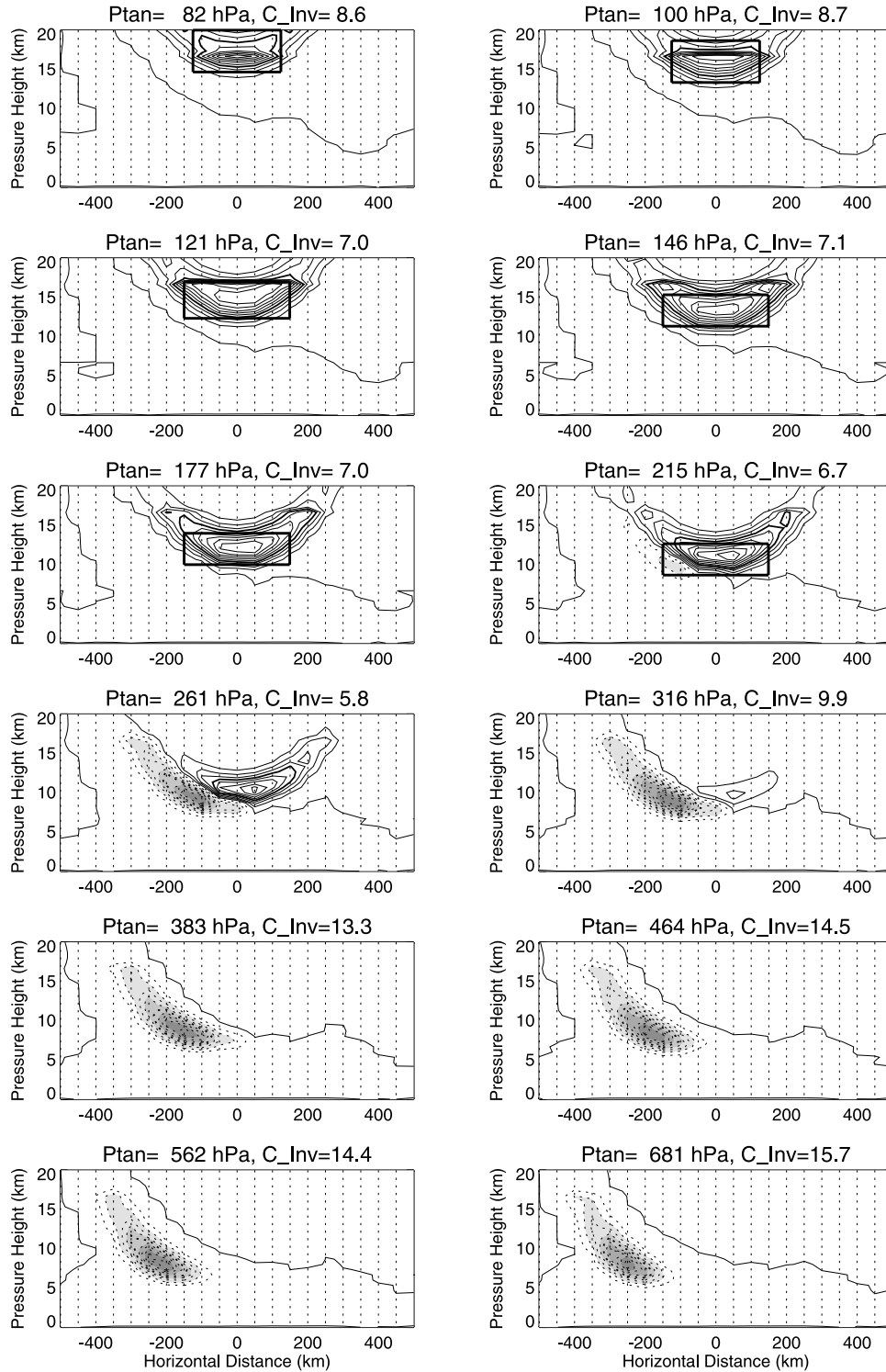
Figure 4. IWC weighting functions (in K•g^{-1}m^3), or $WF(x_i, z_k, P_{tan}, IWC_0)$, for the 2-D RT model (equation (2)) linearized at $IWC_0 = 10$ mg/m^3. The 2-D model has 21 IWC profiles (of which the location is indicated by the vertical dotted lines) and 35 vertical levels (24 levels per decade pressure in hPa). Solid (shaded and dotted) contours show the positive (negative) weights with the contour interval (in K•g^{-1}m^3) indicated in the title of each panel. In this example, MLS views from the negative distance side and is only sensitive to clouds on the MLS side of tangent point at low h_t where the radiance cannot penetrate through the limb. For this calculation a uniform distribution ($IWC_0 = 10$ mg/m^3) is assumed up to ~83 hPa but drops to zero sharply above that pressure level. Contributions at pressures <74 hPa (~18 km) are zeroed in these plots because clouds rarely exceed that altitude.
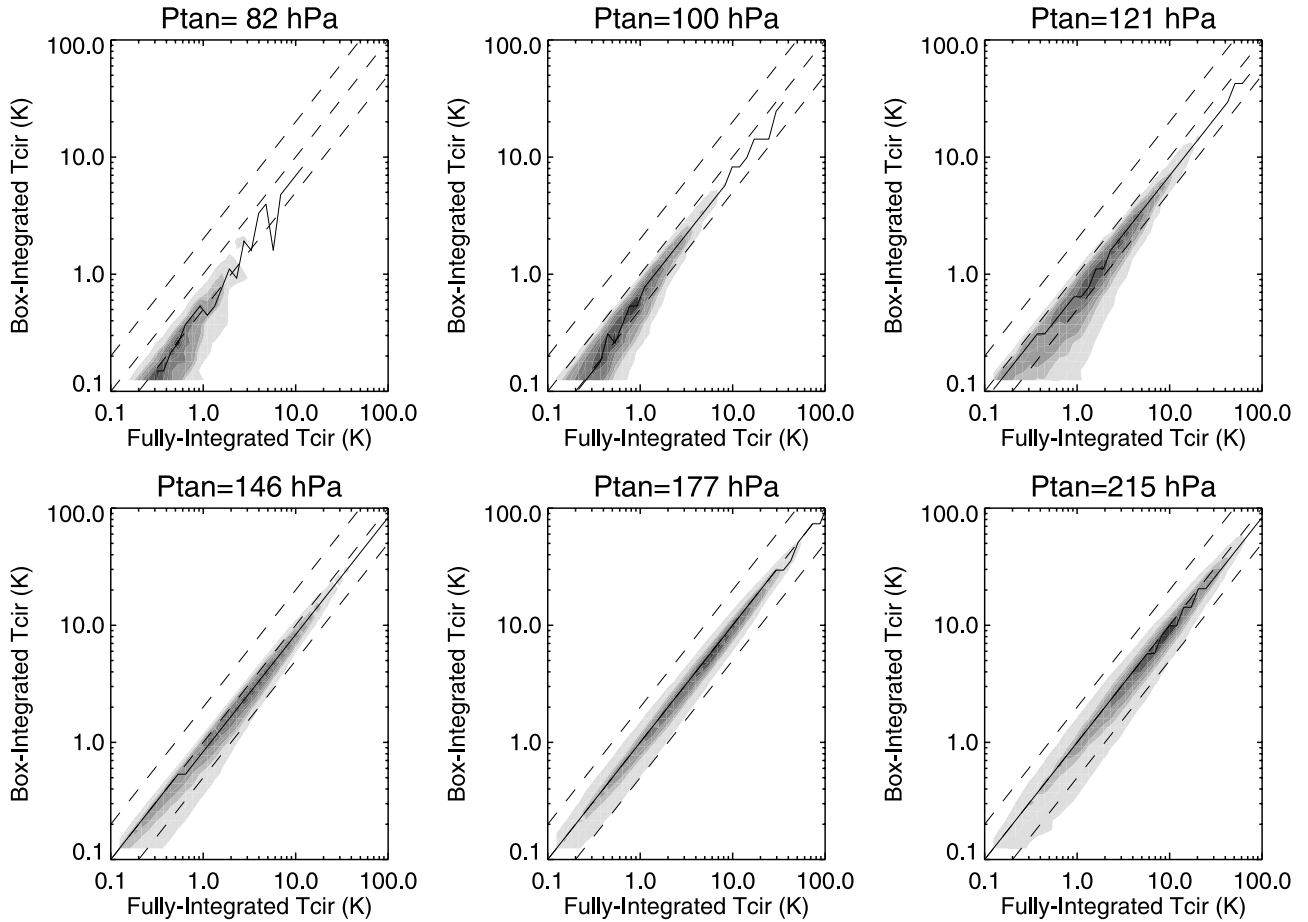
Figure 5. Comparisons of *Tcir* computed from the full 2-D WF and from the 2-D box averaging for six tangent pressures between 83 and 215 hPa. The number density distribution is shaded with the maxima connected by the solid line. The dashed lines indicate ratios of 2:1, 1:1 and 1:2.

binning *Tcir* vertically into the standard 12-levels-per-decade grid does not degrade IWC vertical resolution.

2.5. MLS IWC Data Quality and Screening

[27] The V2.2 IWC are reported in the HDF-EOS (version 5) Level 2 Geophysical Product (L2GP) IWC file under the swath name of IWC with units of g/m^3. The standard IWC product has a useful vertical range between 261 and 68 hPa. In the L2GP file, along with the data value field, IWC precisions are provided but they are estimated values from one test day and are identical in all IWC files. These precisions are rough estimates and the user should screen the data and compute a more accurate precision on a daily basis (discussed in the next two paragraphs). The other IWC quality fields, "Status," "Quality," and "Convergence" in the V2.2 IWC L2GP file are not defined. To exclude IWC measurements affected by bad pointing retrievals, the user is recommended to check the "Status" of the corresponding temperature profile for data quality, and use only profiles with the temperature "Status" equal to an even number [*Schwartz et al.*, 2008]. The L2GP file also reports an IWP product in the IWC L2GP file but under a separate swath, named "IWP," which is retrieved from the 240 GHz *Tcir* at low tangent heights. This IWP is a partial column of cloud ice above ~6 km and will be validated in a separate paper.

[28] The MLS IWC in the L2GP file contains negative values, as expected for any noisy measurements. No cloud mask or screening is applied to the L2GP data. These negative values are retained and needed to properly produce average values, as well as to estimate the IWC precision and bias. The user is required to screen the data to determine if each IWC measurement is significant as a cloud.

[29] To screen the data, the user needs to compute a latitude-dependent IWC precision (σ) and bias (μ), for which we recommend a method (the so-called $2\sigma-3\sigma$ screening) that has been successfully used by the MLS team on the daily IWC measurements. The $2\sigma-3\sigma$ method can be implemented as follows. First, compute and remove latitudinally varying IWC biases at each pressure level. Since the occurrence frequency of MLS clouds is generally less than 20%, one may determine the σ and μ for a given latitude bin (say, 10° wide) by iteratively rejecting the outliers greater than 2σ. The iteration may start with $\mu = 0$ and use all measurements in the latitude bin to compute the first σ. In the next iteration, reject the measurements that differ from μ by more than 2σ, and reevaluate σ and μ from the remaining measurements. The 2σ threshold for estimating μ is somewhat empirically chosen, but the result does not change very much between $2\sigma-4\sigma$ because of the large percentage difference between cloudy and clear measurements at these microwave frequencies. Repeat these steps
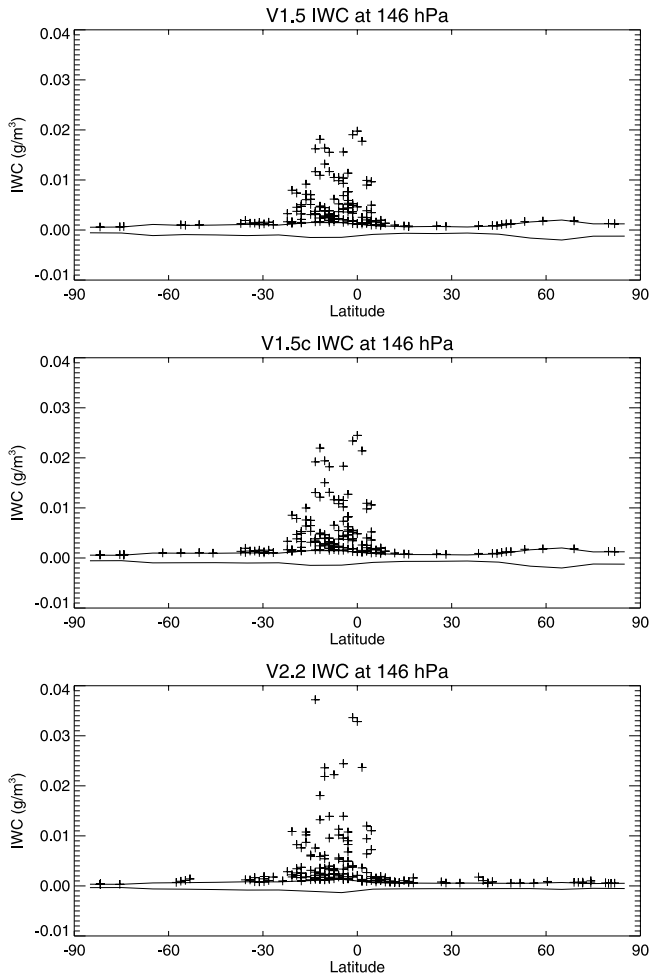
Figure 6. Latitudinal distribution of MLS v1.5, v1.5c, and V2.2 IWC at 147 hPa on 28 January 2005. A latitudinally dependent bias has been removed in these plots. The solid curves are the 3σ envelopes for clear-sky noise and IWC measurements above the 3σ threshold are significant cloud hits.

until the solutions to σ and μ are converged. The convergence is usually reached within 3–10 iterations. The final σ and μ are used as the IWC precision and bias for this latitude bin. Second, interpolate the σ and μ obtained for different latitude bins to obtain the bias at each measurement latitude, and remove the measurement bias using the interpolated μ. In the final step, use the interpolated σ by applying the 3σ threshold to determine the significance of each IWC measurement. In other words, the measurements with IWC $> \mu + 3\sigma$ are significant as clouds. The 3σ threshold is necessary since a small percentage (1%) of clear-sky noise can yield a large percentage error in cloud statistics.

2.6. V1.5 and V2.2 Differences

[30] There are two major differences between V1.5 and V2.2 IWC retrievals. The first is in the RT model. Several improvements, including spectroscopy and instrument parameters, are made in the V2.2 model to produce a better precision for *Tcir* and IWC. The second difference is related to the *Tcir*-IWC relation. The V2.2 relation accounts for

nonlinearity whereas the one in V1.5 is linear. As a result, the V1.5 retrieval systematically underestimates IWC at large values. For this validation study, we also developed an intermediate IWC retrieval (called V1.5c) based on the V1.5 data, which possesses the noise characteristics similar to V1.5 but incorporates the nonlinearity correction as in V2.2.

[31] Figure 6 compares V1.5, V1.5c, and V2.2 IWC retrievals from 28 January 2005 at 147 hPa. The bias has been removed for all of these data sets using the 2σ–3σ screening method described above. On this particular day the V1.5 and V1.5c 3σ envelopes show significantly larger (or worse) values at most latitudes than those of V2.2 IWC, implying a better IWC precision and cloud detectability with V2.2. In addition, the V2.2 3σ envelope is more uniform at middle and high latitudes, whereas the V1.5 precision is noticeably worse at wintertime. As expected, the V1.5c data have a similar precision to that in V1.5, but produce more measurements at IWC > 20 mg/m^3.

[32] Figure 7 compares the normalized probability density functions (PDFs) of V1.5, V1.5c and V2.2 IWC for the January–February period at five latitude bins and three pressure levels. Measurement noise and cloud statistics are reflected in these PDFs. The sharply rising PDF at small IWC values is due to measurement noise. To examine MLS IWC noise more closely, we fold the PDF of negative IWC (called PDF$_n$) to the positive side to illustrate the significance of cloud PDFs. Cloud PDFs must rise above PDF$_n$ in order to be significant. As expected for noise, the PDF$_n$ and the rising PDF at small positive IWC values are alike, showing a Gaussian-type distribution. Comparing the V1.5 and V2.2 PDFs at small values, one can find that V2.2 IWC has a significantly better precision than V1.5 IWC, particularly at high latitudes and at pressures <147 hPa. A better precision also means better ability to detect clouds. At large IWCs, V1.5c exhibits a cloud PDF tail closer to V2.2 as expected from the correction made for the *Tcir*-IWC nonlinearity. The IWC noise varies slightly with latitude and is generally larger in the tropics. The noise at winter high latitudes is slightly higher than that at summer latitudes, as expected for impacts of larger wintertime variability.

3. Estimated Precision and Systematic Uncertainties

3.1. *Tcir* Bias and Precision

[33] Uncertainties of the derived 240 GHz *Tcir*, attributed to either the measured [*Jarnot et al.*, 2006] or the modeled [*Read et al.*, 2006] radiance errors, are often dominated by the model errors. *Tcir* bias and precision (μ_{tcir} and σ_{tcir}) can be estimated empirically from data using the 2σ–3σ screening method described for IWC, and the results from the V2.2 retrieval and from the V2.2 simulation are shown in Figure 8. The *Tcir* errors are characterized separately for the tropical (30°S–30°N) and extratropical (30–82°) bins. At 15 km, both tropical and extratropical PDFs for V2.2 *Tcir* (Figures 8a and 8c) exhibit a Gaussian-like distribution at small *Tcir* values. As expected for noise, the *Tcir* PDF$_n$ in Figure 8a behaves like a Gaussian distribution. In the extratropical case (Figure 8c), the PDF$_n$ obeys the Gaussian law as well but starts to deviate from it at *Tcir* < −1.5 K. The non-Gaussian behavior in the PDF$_n$ implies greater
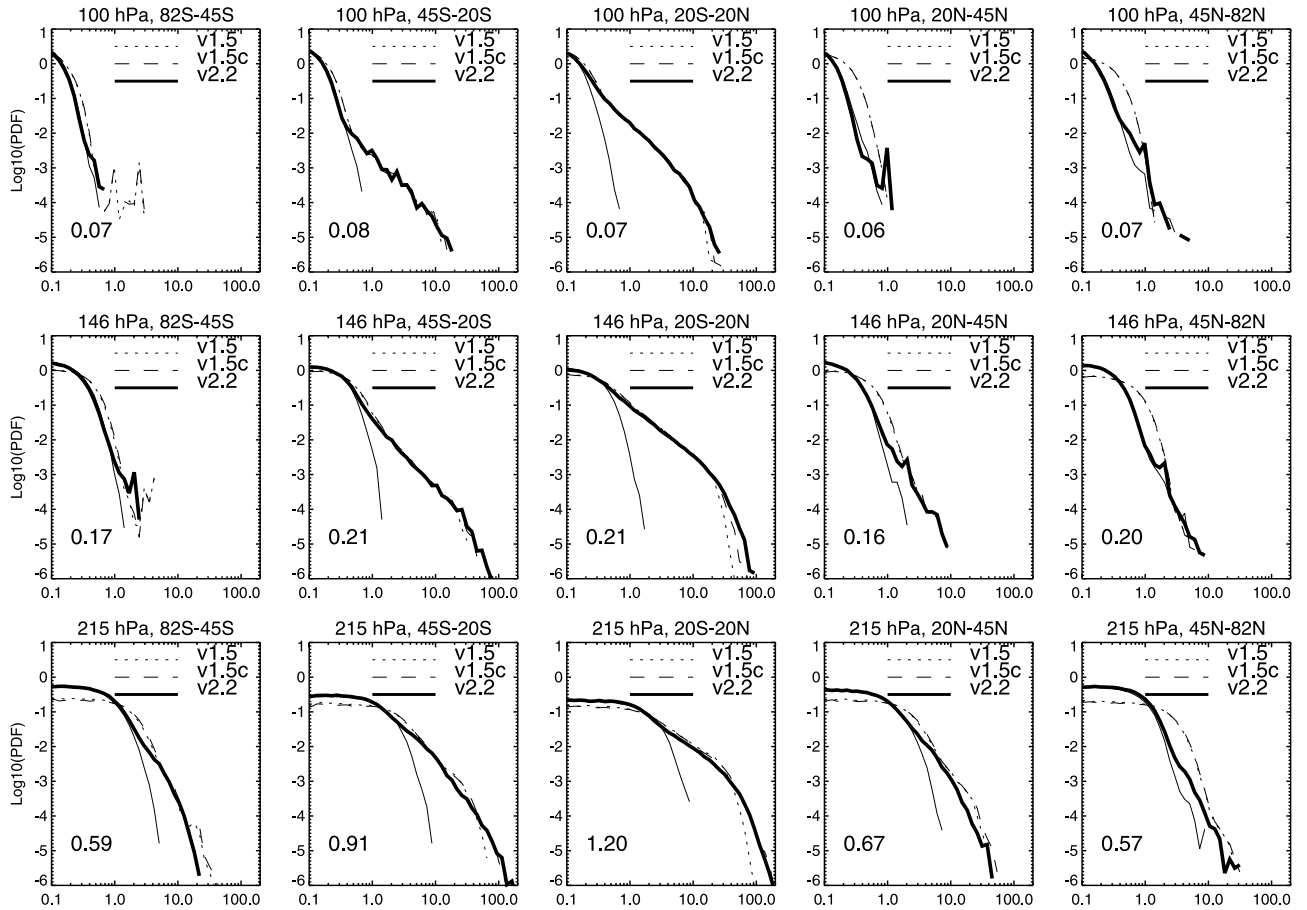
Figure 7. Normalized PDFs of MLS V1.5 (dotted), V1.5c (dashed), and V2.2 (thick solid) IWCs for the January–February period in 2005 and 2006. About 169 and 157 d of V1.5 and V2.2 data are compiled, respectively. The selected results are shown for five latitude bins and three pressure levels. IWC biases are removed in these calculations using the method described in the text. The thin solid line in each panel is the PDF of negative V2.2 IWC (PDF$_n$), but is folded to the positive side to show the noise level. The V2.2 IWC PDF (thick solid line) becomes statistically insignificant where it is near or below the thin line. The estimated standard deviation for the V2.2 IWC (in mg/m^3) is indicated in each panel.

probability of false cloud detection than suggested by the standard deviation. In both tropical and extratropical cases, *Tcir* precisions (0.45 K and 0.38 K, respectively) are larger than the calibrated radiance precision (0.15 K), indicating dominance of the modeled radiance error. Comparing the retrievals for real and simulated data with V2.2 software (Figures 8b and 8d), we find that the algorithm generally produces a better precision for the simulated data than for the real data; but in both cases the *Tcir* precision is worst at $h_t = \sim 8$ km where *Tcir* interferes largely with clear-sky variability.

[34] The V2.2 *Tcir* shows a large (-13 K) negative bias in the tropical bin, and it is somewhat smaller (-6 K) in the extratropical bin (Figure 8b). The V2.2 algorithm corrected this *Tcir* bias prior to the IWC retrieval (Table 1), but used the same bias profile for all latitudes. Therefore, a small latitude-dependent bias remains in the *Tcir* data and is likely propagated to the IWC retrieval. Therefore, the user needs to remove a latitude-dependent bias on a daily basis using the screening method described in section 2.5.

[35] We conducted a series of sensitivity tests to investigate the cause of the negative bias in the 240-GHz *Tcir*.

Various families of uncertainty tests were generated to assess the *Tcir* error, including R2-R3 FOV offset, R1-R3 FOV offset, sideband ratios, gain compression, standing waves from calibration sources, scan jitter, antenna transmission, FOV shape, and spectroscopy. More details about these systematic errors are given by *Read et al.* [2007, Appendix B]. In these end-to-end retrieval tests we evaluated the induced limb radiance errors by perturbing instrumental and RT model parameters within their uncertainties. In addition, we carried out two more sensitivity studies that explore impacts of the T and H_2O retrieval errors. Because the V2.2 algorithm caps the tropospheric *RHi* at 110% in the *Tcir* calculations, the T retrieval error can induce systematic *Tcir* errors through the *RHi* capping even though the H_2O mixing ratio retrieval is perfect. In fact, the H_2O retrieval may have a bias of 20–30% in the upper troposphere [*Read et al.*, 2007]. The derived 240-GHz *Tcir* is particularly sensitive to T and H_2O errors at $h_t = 6-12$ km where its sensitivity to H_2O maximizes. In one test, we perturb the T profile by -2 K as expected for the T retrieval bias [*Schwartz et al.*, 2008]. In the other test, we reduce the
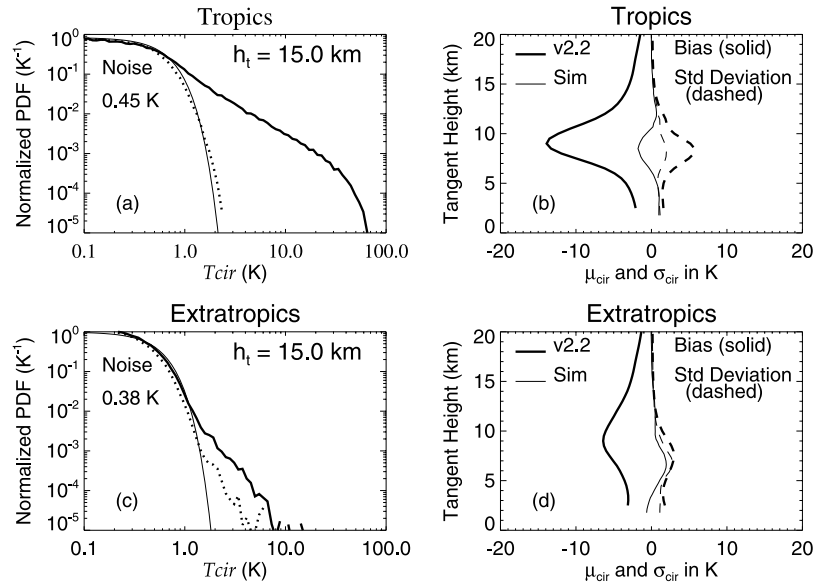
Figure 8. (a) PDF of V2.2 MLS 240-GHz *Tcir* at 15 km tangent height for the tropics (30°S–30°N). The thick solid curve is the PDF of positive *Tcir* whereas the dotted curve is the PDF of negative *Tcir* but folded onto the positive side to compare with the *Tcir* noise fitted by a Gaussian function (thin line). The standard deviation of the Gaussian noise is indicated in the panel. A total of 92 d of data are analyzed and *Tcir* biases have been removed from the daily measurements. (b) Profiles of V2.2 240-GHz *Tcir* bias μ_{cir} (solid lines) and standard deviation σ_{cir} (dashed lines) estimated from the real data (thick) and simulation (thin) as a function of tangent height. (c and d) Same as in Figures 8a and 8b except for the extratropics (82–30°S and 30–82°N).

RHi value by −30% in the troposphere corresponding to the worst retrieval bias [*Read et al.*, 2007].

[36] Only the sources shown in Figure 9 produce a significant error in *Tcir*. The R2-R3 offset and dry-air continuum errors can induce significant (−3 K and +2 K, respectively) *Tcir* biases, which are still too small to explain the observed negative bias. Systematic errors from the retrieved *T* and H_2O, especially both combined, are capable of generating the observed large negative *Tcir* error although the bias peaks at a slightly lower tangent height than observed. We find that the *Tcir* bias is very sensitive to the *T* retrieval error at 10–12 km. As shown in Figure 9, the
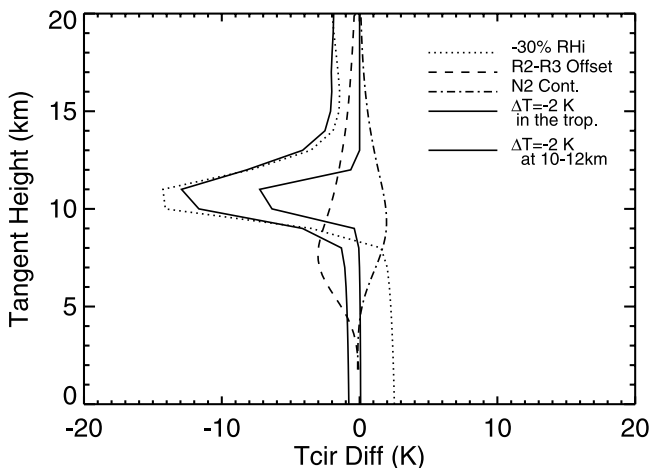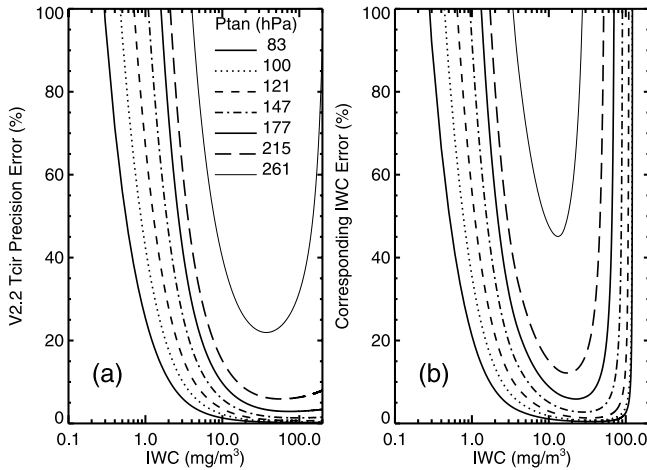
error in the 10–12 km layer contributes −7 K to the *Tcir* bias, compared to −13 K if the entire troposphere is perturbed. MLS *T* retrieval uncertainty remains as a major error source for the derived *Tcir* because the *T* error is semirandom with a vertical correlation length of 2–3 km in the upper troposphere [*Schwartz et al.*, 2008]. As a result, the vertically correlated *T* error (∼1 K) can induce a ∼3 K *Tcir* error at 215 hPa, which is consistent with the precision estimate from the real data (Figure 8).

3.2. IWC Precision

[37] All *Tcir* errors will be propagated directly into IWC through the *Tcir*-to-IWC conversion. A small *Tcir* error can cause a large IWC uncertainty in the nonlinear range where *Tcir* becomes nearly saturated. Figure 10 plots the percentage error of *Tcir* and IWC as a function of IWC. The range where a single V2.2 IWC measurement is quantitatively useful is defined here as IWC percentage error <100%. At small values, the measurement noise is the determining factor. Each IWC measurement must be larger than the 3σ noise to be statistically significant. At large IWC values, the *Tcir* saturation causes great uncertainty in the retrieved IWC as a small *Tcir* error can correspond to a large IWC error. Large IWC values, though associated with an uncertainty > 100%, are still qualitatively useful. At 261 hPa the IWC measurements are mostly qualitatively useful because the IWC percentage error exceeds 100% at IWC > 30 mg/m³ while IWC < ∼12 mg/m³ are mostly noise. Hence, our validation studies will focus mainly on pressure levels at 215–83 hPa.

[38] Table 2 summarizes typical single-measurement precisions and useful ranges of the V2.2 IWC for different pressure levels. The user needs to obtain a more accurate

Figure 9. Systematic uncertainties estimated for MLS 240-GHz *Tcir* due to errors in *T*, *RHi*, R2-R3 pointing offset, and dry continuum.

Figure 10. (a) Estimated V2.2 *Tcir* precision as a function of IWC in percentage for different tangent pressures. (b) Estimated V2.2 IWC precision as a function of IWC in percentage.

precision estimate using the aforementioned screening method on a daily basis. The V2.2 IWC precision increases with pressure, which is consistent with the value expected from the *Tcir* error in Figure 8. In Table 2 the V1.5 and V1.5c precisions are similar, both worse than the V2.2 precision.

3.3. IWC Systematic Uncertainties

[39] In this section we will study IWC systematic uncertainties for values <50 mg/m³. Various error sources from models as well as from the measurement are discussed.

3.3.1. Effects of Cloud Inhomogeneity

[40] The modeled *Tcir*-IWC relations used in V2.2 are based on the 1-D model simulations for a layered cloud where MLS FOV and cloud inhomogeneity are ignored. Cloud inhomogeneity, especially one along the LOS, can affect the accuracy and meaning of the retrieved MLS IWC. If the cloud field is broken along the LOS but transparent to the MLS frequency, the averaged IWC as defined for the resolution box (Figure 4) will still be accurate since all broken clouds are within the linear regime of the *Tcir*-IWC conversion. However, if some of the broken clouds are optically thick and underestimated by the *Tcir*-IWC conversion, the retrieved IWC will produce a bias in cloud ice averaged over the box. A similar discussion on cloud inhomogeneity effects is given by *Davis et al.* [2007].

[41] To assess IWC uncertainties induced by cloud inhomogeneity, we need to know realistic distributions of the IWC inhomogeneity. This requires large statistics of IWC variability over hundreds of kilometers in distance with vertical resolution better than 1 km, which are not readily available with airborne and sground-based observations. Because MLS measurements involve large FOV and limb-view averaging, cloud spatial variability is more important than temporal variability for interpreting the results. Also, ground-based observations are not quite useful for our study since connection between spatial and temporal inhomogeneity requires additional assumptions about cloud variability. Thus, for this study we use CloudSat IWC observations

to assess cloud inhomogeneity effects on MLS V2.2 IWC retrieval.

[42] With the CloudSat IWC profiles along the A-Train track, we simulated MLS 240-GHz *Tcir* using the MLS 2-D RT model and compared the derived *Tcir*-IWC relations with those used by V2.2. We randomly selected 2000 cases from CloudSat data in January 2007, binned the CloudSat IWC profiles into the input grid sizes (0.5° horizontally and ∼0.67 km vertically) of MLS 2-D model, computed MLS *Tcir*, and compared the *Tcir* to the IWC averaged over the volume boxes in Figure 4. The resulting *Tcir*-IWC relations are shown in Figure 11 and compared to the V2.2 relations.

[43] As shown in Figure 11, the selected CloudSat cases cover a broad range of IWC values. The *Tcir*-IWC scatter reflects the uncertainty of individual V2.2 IWC measurements due to cloud inhomogeneity. As discussed above, interpreting V2.2 IWC as an average in the volume box near the tangent point may induce error. However, to first order, the inhomogeneity-induced IWC uncertainty appears to be random and can be reduced by averaging (e.g., monthly maps). For example, on a grid box of 5° × 10° latitude-longitude, Aura MLS typically has a total of ∼80 samples in the tropics during a month, which could reduce inhomogeneity-induced uncertainty by a factor of 9 if averaged. The inhomogeneity-induced percentage error tends to increase at smaller *Tcir* values or at higher pressures, but less scatter is found for the simulations at 147 and 177 hPa than at other pressure levels. The inhomogeneity error can be corrected properly with a 2-D tomographic IWC retrieval on MLS *Tcir*, the technique currently used in MLS clear-sky gas retrievals [*Livesey et al.*, 2006]. Such an IWC retrieval is currently being developed for a future version of MLS retrieval algorithm.

[44] Figure 11 also reveals an inhomogeneity-induced scaling error in the V2.2 *Tcir*-IWC relations (equation (1)), which cannot be reduced by averaging. The scaling error is pressure-dependent, generally less than 30% at 177−121 hPa but can be as large as −70% at 100−83 hPa for the retrieved IWC. It is also latitude-dependent, especially at 177 and 215 hPa, showing that the *Tcir*-IWC relations have a smaller slope in the extratropical bin. At 215 hPa, ignoring cloud inhomogeneity, the V2.2 retrieval would overestimate IWC by 80% in the tropics but under-

Table 2. Estimated MLS IWC Precision and Useful Range

| Pressure, hPa | Precision, mg/m³ | | | | IWC Range,[c] mg/m³ |
	V1.5[a]	V1.5c[a]	V2.2[a]	Simulation[b]	
83	0.08−0.14	0.08−0.15	0.06	0.09	0.02−120
100	0.1−0.15	0.1−0.16	0.07	0.1	0.02−120
121	0.14−0.2	0.14−0.2	0.1	0.1−0.2	0.04−110
147	0.3−0.4	0.3−0.4	0.2	0.3−0.5	0.1−90
177	0.6−0.9	0.7−0.9	0.3−0.6	0.6−1	0.3−70
215	1.2−1.8	1.3−1.9	0.6−1.3	1−1.6	0.6−50

[a]These are typical 1σ precisions estimated for MLS data, where the better precision values are for the extratropics and the poorer values for the tropics. The precision for a particular measurement must be evaluated on a daily basis using the method described in the text.
[b]These are the estimates of IWC precision from the simulation test. The range reflects differences between the tropical and extratropical retrievals.
[c]A V2.2 IWC measurement is considered to be quantitatively useful if it is statistically significant and its precision is less than 100%. The useful range for a single V2.2 IWC measurement is limited by the uncertainty (2σ) about IWC biases from the screening method and by the *Tcir* saturation at the high end.
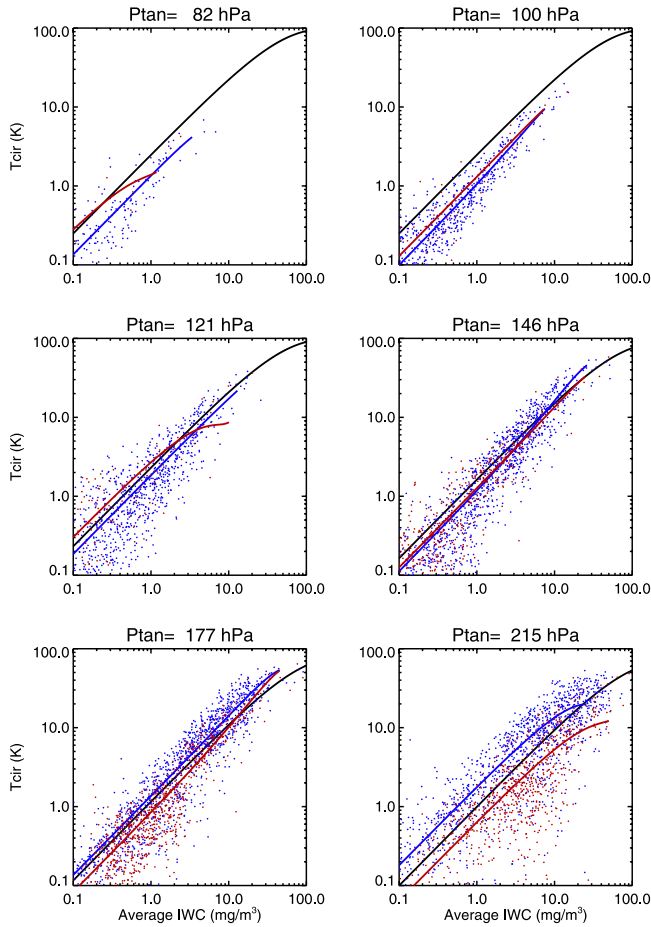
Figure 11. Comparison of the V2.2 *Tcir*-IWC relations (black curves) with those modeled by the 2-D RT model using CloudSat IWC profiles (dots). A total of 2000 randomly selected CloudSat cases are used for the simulation: 1229 (red) from the tropics ($20°S-20°N$) and 771 (blue) from the extratropics. The IWC is averaged over the rectangular boxes as depicted in Figure 4. The colored curves correspond to the polynomial fit to the simulated *Tcir*-IWC relations in each latitude bin, and only data with IWC > 0.1 mg/m^3 are used in the fitting.

estimate it by 40% in the extratropics, and the underestimation becomes worse for large IWC values. At 147 and 177 hPa, the V2.2 retrieval tends to underestimate IWC at values <10 mg/m^3 but overestimate it at values > 10 mg/m^3, and the overestimation appears to increase with IWC at large values.

3.3.2. Uncertainties due to Particle Size Distribution

[45] To assess PSD uncertainties, we perturb parameters of the MH97 PSD by 2σ of their uncertainty and calculate the changes in *Tcir* and IWC from these perturbations. The calculated root-square sum (RSS) of the *Tcir* and IWC changes are reported as a function of IWC. As shown in Figure 12 the resulting *Tcir* and IWC changes are generally less than 40% in the linear regime of the *Tcir*-IWC relations. The IWC uncertainty increases sharply as *Tcir* approaches saturation. It exceeds 100% when IWC is greater than 30,

65, 100, 120, 160, 190, and 200 mg/m^3 at 261, 215, 177, 147, 121, 100, and 83 hPa, respectively.

[46] To evaluate uncertainty of the modeled *Tcir*-IWC relation due to different PSDs, we studied four parameterization schemes (MH97) [*Heymsfield et al.*, 2002; *Donovan and van Lammeren*, 2002; *Field et al.*, 2005], which represent a variety of methods and clouds. Because at MLS frequencies the *Tcir* is sensitive to ice particles of relative large sizes ($>\sim100 \mu$m), the IWC retrieval relies on a modeled PSD to partition between total ice amount and the part sensible to MLS. Thus, the MLS *Tcir*-IWC relation is sensitive to the slope of parameterized PSDs at sizes > $\sim100 \mu$m as well as the relative mass contribution from those < $\sim100 \mu$m. Various schemes produce significantly different PSD slopes and partitions for these sizes.

[47] The MH97 PSD parameterization, used in the MLS IWC retrieval, is based on in situ measured size distributions at $20°S-2°N$ latitudes, mostly from cirrus outflows. The size variable is the mass-equivalent diameter (D). As a function of T and IWC, the MH97 parameterization can produce a bimodal distribution and is valid for $-70°C < T < -20°C$. Bimodal PSDs, which further complicate microphysics of ice clouds [e.g., *Platt*, 1997], play a critical role in IWC remote sensing because cloud ice masses associated with the two modes are equally important and MLS 240 GHz measurement is mostly sensitive to *Tcir* induced by the large particle mode [*Wu and Jiang*, 2004]. *Heymsfield et al.* [2002] (hereinafter referred to as H02) fit the in situ data collected in the tropics and subtropics to a single Gamma distribution as a function of particle maximum dimension (D_m). The resulting PSDs also depend on T and IWC but are only valid for $T > -50°C$ with the best results for $-40°C < T < 0°C$. Comparing to MH97, H02 should have a better size distribution parameterization for particle sizes > 2 mm. *Donovan and van Lammeren* [2002] (hereinafter referred to as DL02) developed a bimodal PSD parameterization using lidar-radar remote sensing data at the Atmospheric Radiation Measurement Program's Southern Great Plains (ARM-SGP) (36.4°N). The size variable is D_m and the parameterized PSD is valid for $T > -50°C$. *Field et al.* [2005] (hereinafter referred to as F05) developed a bimodal PSD based on the in situ data (at $D_m > 100 \mu$m) acquired around the British Isles. It is valid for midlatitude clouds at $T > -50°C$. Unlike the other three studies, this parameterization should be viewed with caution in the deduced *Tcir*-IWC relation since the IWC contribution from particles of $D_m < 100 \mu$m is not constrained by observations.

[48] Because the PSD parameterizations other than the MH97 are limited to temperatures > $-50°C$, we focus only on the error assessment at 215 hPa (or $-50°C$). To compare these different PSD parameterization schemes, we assume the mass-diameter relation described by *Brown and Francis* [1995], and convert D_m to D (mass equivalent diameter) when needed. At this level, the modeled *Tcir*-IWC relations for H02 and DL02 have a steeper (50% and 100%, respectively) slope in the linear region than MH97, meaning that the H02 and DL02 PSDs would yield a smaller IWC by the similar percentages. The modeled slope for F05, steeper by 200%, deviates further from the MH97 *Tcir*-IWC relation, which would reduce the retrieved MLS IWC more. The PSD parameterizations other than MH97 imply that the
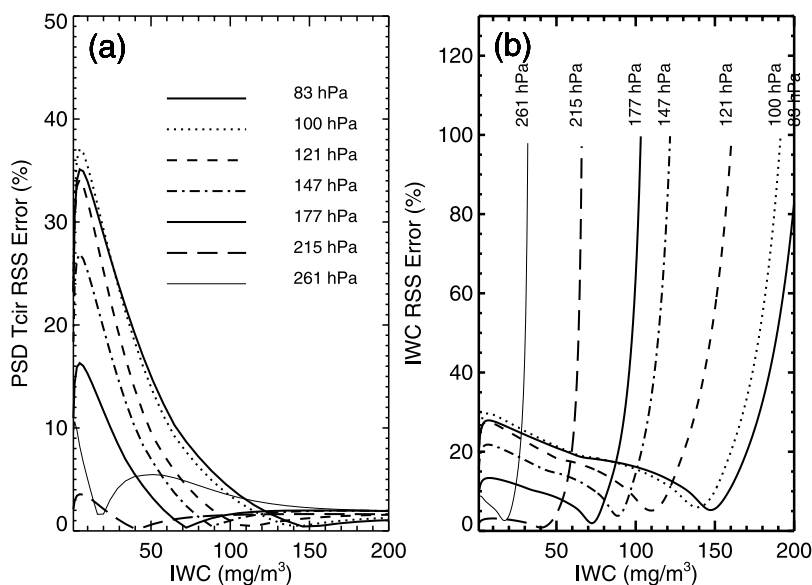
Figure 12. RSS of relative uncertainty (%) of the modeled *Tcir*-IWC relation due to error in MH97 PSD fitted parameters as a function of IWC: (a) *Tcir* and (b) IWC.

MLS IWC retrieval (based on the MH97 PSD) might be too high at 215 hPa. As seen later in MLS-CloudSat comparisons, the implication from the other PSD parameterizations would make MLS IWC deviate more from the CloudSat IWC retrieval. Since both H02 and DL02 are based on tropical and subtropical clouds, the percentage differences relative to MH97 reflect uncertainty due to different parameterization schemes. Furthermore, the larger percentage difference between F05 and MH97 could result from sampling differences between midlatitude (F05) and tropical (MH97) clouds, but the large uncertainty of F05 PSD at $D_m < 100$ μm remains to be quantified. Therefore, our conservative estimate for the PSD-induced uncertainty in the modeled *Tcir*-IWC relation would be 100%.

[49] At pressures ≤ 147 hPa, the sparsity of in situ PSD measurements is even more severe, which is expected to yield larger uncertainty in the MH97 parameterization than at 215 hPa. For example, in situ PSD measurements may be biased toward certain types of high clouds (i.e., cirrus outflows in the MH97 case), not applicable for strong deep convective clouds. To assess impacts of convection-perturbed PSDs, we conducted a sensitivity study by manipulating the temperature dependence in the MH97 parameterization. In this test, we replace the MH97 PSD parameters at -75°C with ones at -60°C, as a presumable change due to deep convection. We found that changing PSD characteristics would lead to a $\sim$30% error in the modeled *Tcir*-IWC relation at -75°C. This error would be larger if the clouds were lifted from a lower altitude.

3.3.3. Uncertainty due to Particle Shapes

[50] The modeled *Tcir*-IWC relation can also be affected by uncertainty about ice particle habits or shapes that make *Tcir* polarization-dependent. The MLS IWC retrieval currently neglects polarization differences by assuming spherical particles, and here we evaluate potential errors due to this assumption. *Evans and Stephens* [1995] found that different particle habits may induce a factor of $2-3$ differences in volume extinction coefficients compared to spher-

ical particle results, but the differences reduce to 100% in the derived *Tcir*-IWP relation for the worst scenario (i.e., consisting of all nonspherical particles aligning in the same orientation). In reality, large ice particles in the upper troposphere are associated with strong turbulence, and these nonspherical particles are likely to orient themselves semi-randomly. Analyzing the 122 GHz *Tcir* observed by Aura MLS, *Davis et al.* [2005b] found that the polarization differences are generally less than 10% of the observed *Tcir* values. Using the 3D RT cloudy-sky model developed by *Davis et al.* [2005a], *Davis et al.* [2005b] found that the aspect ratio of 1.3 fit best to the observed polarization differences at 122 GHz. Using the same aspect ratio, we modeled the polarized *Tcir* differences at 240 GHz and found that they are generally less than 20% at $h_t > 10$ km for IWC < 200 mg/m^3. Hence, we conclude that particle-shape-induced uncertainty in the V2.2 IWC retrieval is less than 20%.

3.3.4. Other Uncertainties

[51] Mixed-phase clouds may alter the *Tcir*-IWC relation by producing more emitted than scattered radiation inside clouds. Because liquid clouds are much more (170 $\times$ at 240 GHz and -30°C) efficient emitter/absorber than ice, mixing ice and liquid droplets may reduce *Tcir* sensitivity to ice as much as $10-40$% at 240 GHz with liquid water content (LWC) of $10-150$ mg/m^3 up to a -40°C altitude. Mixed-phase clouds occur rarely at $T < -40$°C because liquid droplets would freeze spontaneously [*Hogan et al.*, 2003]. Since most of the mixed-phase clouds are below the valid MLS IWC range, this type of error is unlikely to have significant impacts on the MLS retrieval.

[52] Finally, MLS T retrieval error can cause large uncertainty in the derived *Tcir*. As discussed above in the *Tcir* error section, the T uncertainty ($\sim$3 K at 215 hPa) contributes most to the 240-GHz *Tcir* precision. As shown by *Schwartz et al.* [2008], the T precision exhibits significant geographical variability, and therefore, the screening method used for the V2.2 IWC data will likely produce more

Table 3. Estimated Systematic Uncertainties for MLS V2.2 IWC

	CI RMS Uncertainty[a]		CI Scaling Uncertainty[b]		MH97	Other	Ice	Mixed
Ptan, hPa	0.5–5 K	5–20K	Tropical	Extratropical	Fitting	PSDs[c]	Habits	Phase
83	50%	–	−50%	–	<30%	–	<20%	–
100	50%	40%	−70%	−40%	<30%	–	<20%	–
121	100%	70%	−20%	+20%	<30%	–	<20%	–
147	100%	80%	−30%	−20%	<30%	–	<20%	–
177	150%	80%	+20%	−30%	<30%	–	<20%	–
215	300%	80%	+80%	−40%	<30%	100%	<20%	<40%

[a]These are 2σ RMS (root mean square) errors on a single IWC measurement due to cloud inhomogeneity (CI). They are estimated from the simulated results in Figure 11 and reported for two ranges of Tcir values.

[b]CI-induced scaling errors in the V2.2 Tcir-IWC relations are strongly latitude-dependent. They are estimated separately for the tropical and extratropical bins as defined in Figure 11.

[c]This is uncertainty due to PSD parameterizations other than MH97.

false detections in a noisier region within the same latitude bin. As a result, some artificial clouds with low IWC values may be found in cloud maps, which correlate with large T variability. These artificial clouds usually occur at wintertime high latitudes where stratospheric gravity waves (GWs) cause increased error in MLS T retrieval. The GW-induced T error is reduced substantially in the V2.2 retrieval, which improves cloud detection at high latitudes.

3.3.5. Summary of Systematic Uncertainties

[53] Systematic uncertainties of the V2.2 IWC are summarized in Table 3. Although cloud inhomogeneity can cause large uncertainties on individual IWC measurements, this error is mostly random and can be reduced by averaging the data. The inhomogeneity-induced error will be corrected properly in the future with a 2-D tomographic IWC retrieval. The largest systematic uncertainty in the V2.2 IWC retrieval is from the PSD assumptions used in the cloudy-sky RT models. The MH97 parameterization used for the V2.2 IWC retrieval may not be applicable to deep convective cores nor to midlatitude clouds. The modeled Tcir-IWC relations from different PSDs can differ systematically by as much as 100% at 215 hPa. Currently, we do not have a PSD parameterization that can represent global ice cloud prop-

erties accurately. In situ observations of PSDs remain very sparse and incomplete, resulting in poorly constrained microphysical assumptions used in MLS IWC retrievals. Much work is needed to improve PSD parameterization and statistical properties of global ice clouds.

4. Comparisons With CloudSat

[54] CloudSat is the first spaceborne cloud profiling radar (CPR) that measures vertical structures of clouds and precipitation at 94 GHz [Stephens et al., 2002]. It was launched in April 2006 and currently flies in formation with Aqua, Aura, and CALIPSO satellites as a part of the NASA A-Train. However, the MLS and CloudSat sampling tracks are separated by ∼200 km in most parts of the orbit (Figure 13). This sampling offset makes it difficult to compare MLS and CloudSat IWC measurements directly on a point-by-point basis. In addition, MLS and CloudSat measurements are also separated in time by 7–8 min, which marginally qualifies as "coincident" cloud measurements. Coincident cloud measurements need to be taken in a time period shorter than cloud temporal variability. For example, deep convective systems can raise cloud heights by ∼4 km in
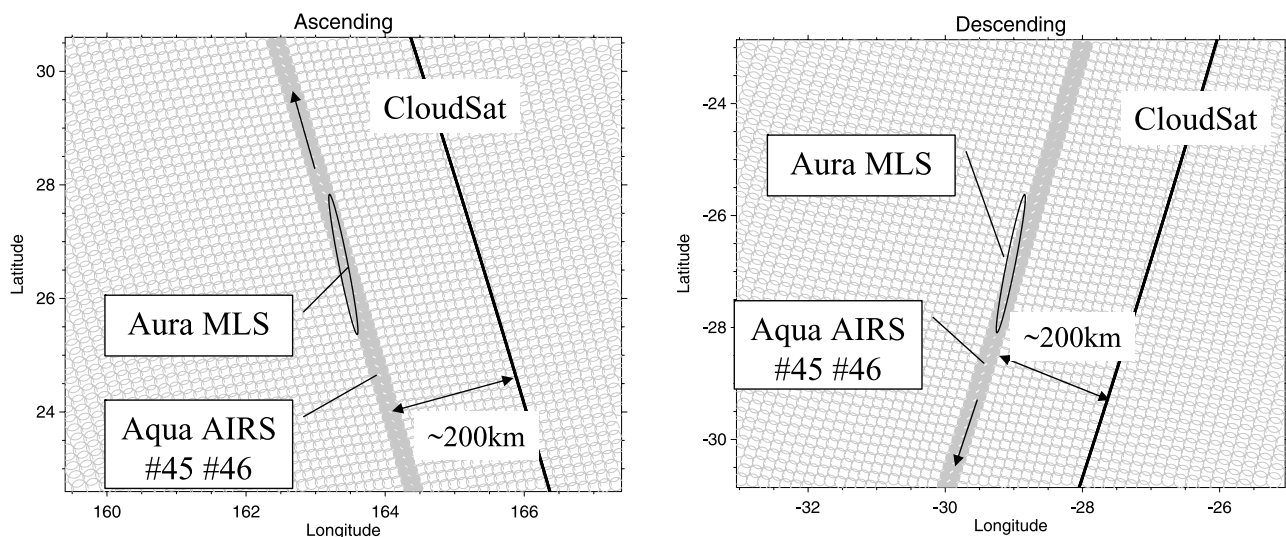
Figure 13. Diagram of MLS, AIRS (Atmosphere Infrared Sounder), and CloudSat sampling tracks as shown under the A-Train configuration on 4 August 2006. The AIRS samples 45 and 46 are used to indicate the Aqua nadir. In this configuration CloudSat is flying in formation with CALIPSO lidar and the latter needs to point slightly off nadir to avoid sun glints, which results in CloudSat footprints ∼200 km off from the Aqua nadir or the Aura MLS tangent footprint (long ellipse) at most latitudes.
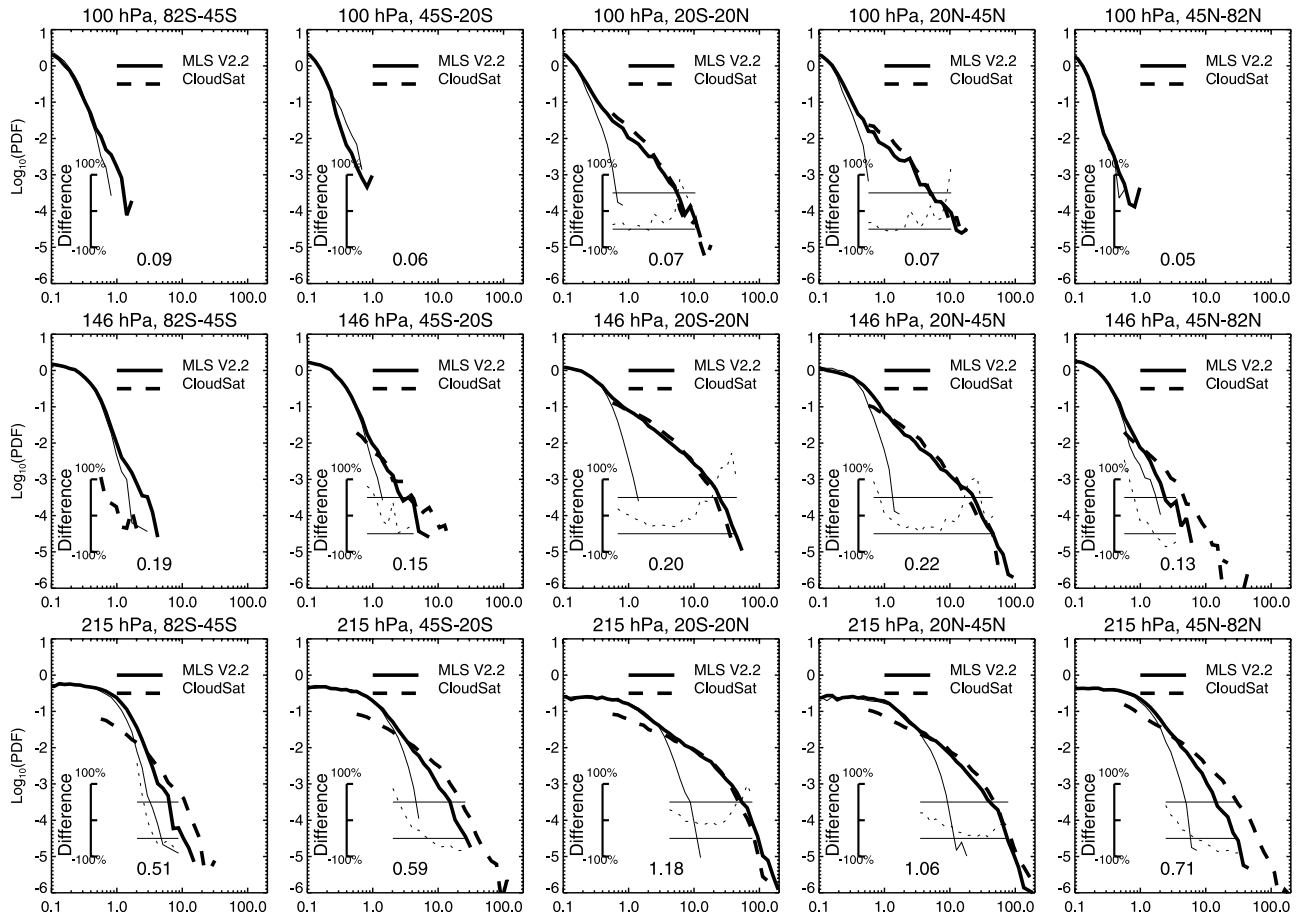
Figure 14. Comparisons of normalized PDF for MLS V2.2 (thick solid) and CloudSat (dashed) IWC in July at different latitude bins and pressure levels. The thin line is the PDF of negative MLS IWC folded to the positive side and the estimated standard deviation σ of V2.2 IWC noise is given in each panel. The rising PDFs at IWC $< 3\sigma$ are mostly contributed by noise. CloudSat IWC PDFs below 5 mg/m^3 should be viewed with caution because of its incomplete noise statistics (see text). Percentage differences of MLS V2.2 PDFs with respect to CloudSat (MLS-CloudSat) are plotted as the dotted line for the range between 3σ and 80 mg/m^3, and the horizontal lines indicate $\pm50\%$. Only PDF differences with significant statistics (i.e., number of samples in an IWC bin > 4) are shown. MLS statistics are based on 61 d from 2005 to 2007, whereas CloudSat statistics are from 31 d of R03 data in July 2006.

7 min with a 10 m/s updraft [*Geerts et al.*, 2000]. Given these sampling differences, we choose to compare statistical properties of MLS and CloudSat IWC measurements.

[55] As a bulk cloud property averaged over a finite volume, IWC can be different from instrument to instrument because of sampling volume differences even when the observed cloud field is identical. Cloud inhomogeneity and transiency often make interpretation of IWC measurements complicated. For proper IWC comparisons, one should first to make the sampling volumes comparable by averaging the finer-resolution data spatially to match the low-resolution data. A CloudSat IWC profile has vertical resolution of 240 m and horizontal resolutions of ~1.4 km (cross-track) by 1.8 km (along-track). The integration time is 0.16 s, which yields a sampling of 1.1 km along track. The 1.8 km along-track resolution is resulted from convolution of the 1.4-km beam width and the 1.1-km integration smearing. In all the MLS-CloudSat comparisons below, we average CloudSat IWC profiles to match the MLS measurement using the rectangular box along track as defined in Figure 4, but we neglect effects of cross-track averaging.

[56] We use the version 3 (R03) CloudSat 2B-IWC product for which the retrieval is based on the techniques described by *Austin and Stephens* [2001] and *Benedetti et al.* [2003]. The 2B-IWC retrieval is limited to daytime because it uses radar reflectivity from CloudSat and visible optical depth from MODIS. A radar-only retrieval, called 2B-IWC-RO, is developed by the CloudSat team to give both day and night measurements. The current 2B-IWC-RO algorithm fits a single spectral width to each radar reflectivity profile, which means that the Gamma distribution shape is same in the entire profile. In the R03 retrieval, IWC is zeroed for temperatures above 0°C and scaled linearly to zero for temperatures between −20°C to 0°C. This product applies a reflectivity threshold for cloud detection before the IWC retrieval, and therefore the IWC statistics below the reflectivity threshold (equivalent to ~5 mg/m^3 in IWC) is not available. The reflectivity threshold yields incomplete IWC statistics by eliminating noise statistics for IWC <
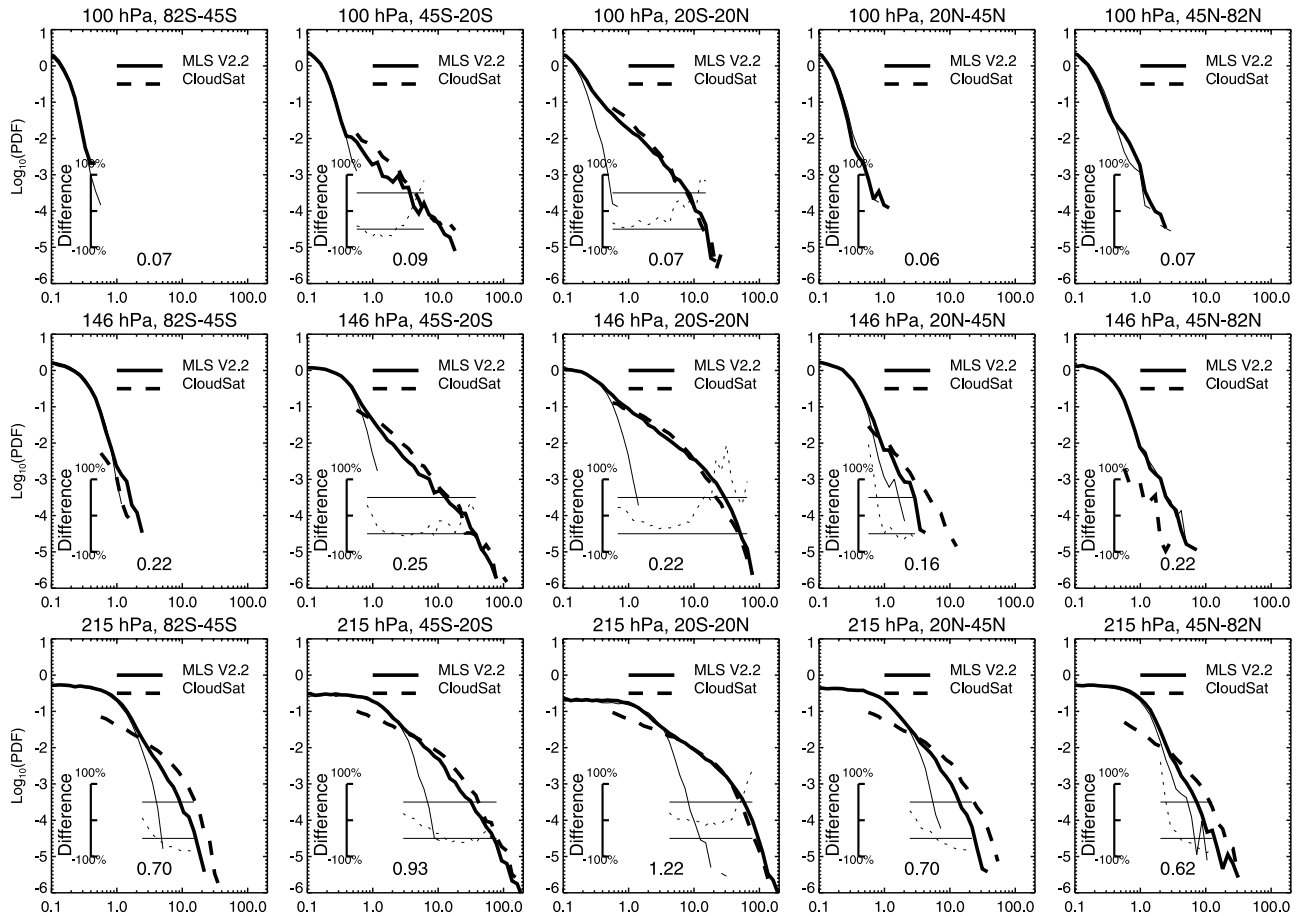
Figure 15. As in Figure 14 but for January. MLS statistics are based on 78 d of V2.2 data in 2005–2007 whereas CloudSat statistics are from 29 d of data in January 2007.

5 mg/m^3. This truncation apparently affects the MLS-CloudSat IWC comparison since some 3200 CloudSat measurements need to be averaged to compare to each MLS measurement. If CloudSat IWC statistics were fully preserved and the noise were purely random without any bias, we could trust the averaged CloudSat IWC down to $5/\sqrt{3200}$ or ∼0.1 mg/m^3. Because CloudSat IWC noise statistics are truncated, the comparison for the IWC < 5 mg/m^3 must be viewed with caution.

[57] In Figures 14 and 15 we compare MLS and CloudSat IWC statistics for January and July at five latitude and six altitude bins in terms of normalized PDF. For MLS V2.2 IWC, we use all the data that have been processed to date for these months in 2005–2007 to improve the statistics. Since interannual variations of IWC PDFs are relatively small (<20%) on the basis of MLS V1.5 observations, the multiyear monthly statistics can be used to characterize overall MLS-CloudSat IWC differences. The PDF method has been used in a number of earlier cloud ice studies [e.g., *Mace et al.*, 2001; *Hogan and Illingworth*, 2003; *van Zadelhoff et al.*, 2004], and was also suggested for tracer gas comparisons in the case where coincident measurements were difficult to obtain [*Lary and Lait*, 2006]. One of the advantages with the PDF method is to allow comparisons of noise, sensitivity, and accuracy collectively. These data attributes are usually mixed together after averaging, and

become difficult to quantify individually from the averaged quantity (e.g., monthly maps).

[58] In Figures 14 and 15 MLS and CloudSat PDFs generally agree well with each other, showing consistent cloud distributions for most latitude and pressure bins over the valid IWC range (i.e., PDF above PDF$_n$). The percentage differences between MLS V2.2 and CloudSat data are generally less than 50% in the valid IWC range. In the tropical bins where IWC < 5 mg/m^3, MLS IWC is lower than CloudSat by ∼50% at 100 and 121 hPa. This is likely due to the inhomogeneity-induced error shown in Figure 11 where the estimated scaling error is between −20% and −70% in the tropics. If this is the case, these MLS-CloudSat differences would be reduced in the future 2-D MLS IWC retrieval. The biases at 215–147 hPa in the tropics are relatively small for IWC < 10 mg/m^3. If we include the inhomogeneity-induced scaling error in MLS V2.2 IWC, the MLS-CloudSat differences could be as large as 80%. All MLS-CloudSat biases tend to increase with IWC from negative to positive, which is consistent with the behavior of the V2.2 scaling error due to cloud inhomogeneity (Figure 11). The V2.2 *Tcir-IWC* relations deviate more from the simulated relations at larger IWC values, showing that V2.2 tends to overestimate IWC at 147 and 177 hPa for values > 10 mg/m^3.

[59] In the high-latitude and high-altitude bins, the MLS PDFs fall down substantially, not much above the PDF$_n$.

Table 4. Summary of Estimated MLS V2.2 IWC Precision, Accuracy, and Resolution

Pressure, hPa	Typical Precision,[a] mg/m^3	Accuracy,[b] %		Resolution[c] H$_\parallel$ × H$_\perp$ × V, km	Valid IWC Range,[d] mg/m^3
		<10 mg/m^3	>10 mg/m^3		
83	0.06	100%	–	200 × 7 × 5	0.02−50
100	0.07	100%	100%	200 × 7 × 5	0.02−50
121	0.1	100%	100%	250 × 7 × 4	0.04−50
147	0.2	100%	100%	300 × 7 × 4	0.1−50
177	0.3−0.6	150%	100%	300 × 7 × 4	0.3−50
215	0.6−1.3	300%	100%	300 × 7 × 4	0.6−50

[a]These are typical 1σ precisions of single IWC measurements where the better values are for the extratropics and the poorer values for the tropics. The precision for a particular measurement must be evaluated on a daily basis using the method described in the text.

[b]Estimated from the V2.2 IWC retrieval uncertainties due to cloud inhomogeneity, modeled *Tcir*-IWC relations, and PSD parameterizations.

[c]H$_5$, H$_2$ and V denote the along-track, cross-track and vertical extent, respectively, of the atmospheric volume sampled by an individual MLS measurement.

[d]This is the range where the stated precision, accuracy and resolution are applied. IWC values above this range, currently giving qualitative information on cloud ice, require further validation for quantitative interpretation.

Because MLS IWC noise can be non-Gaussian (i.e., with a wider distribution at larger IWC values), the 3σ detection will likely introduce a higher percentage of false detections at these latitudes. In some cases (e.g., 146 hPa and 45−82°N) the IWC PDF (based on CloudSat statistics) is below the MLS PDF$_n$, which means that these IWCs are too low and two few for MLS to observe.

[60] Nonetheless, a low (∼70%) MLS bias is evident in high-latitude bins (45−90°N in July or 45−90°S in January) at 215−177 hPa. This low bias, mostly at IWC > 5 mg/m^3, is consistent with the estimate of inhomogeneity-induced V2.2 retrieval error. Figure 11 shows that the V2.2 IWC retrieval may be biased −40% low in the extratropics and the bias may increase with IWC. However, as discussed in section 3.3, the V2.2 IWC retrievals may have a high bias from the MH97 PSD. On the other hand, the single-mode Gamma PSD used by CloudSat may cause additional bias by oversimplifying cloud PSDs in this region [e.g., *Korolev et al.*, 2001; *Delanoë et al.*, 2005]. Thus, it is not clear what really causes the MLS-CloudSat differences at high latitudes. The uncertainty of these IWC retrievals remains quite large compared to those at low latitudes. To reduce this uncertainty, a more accurate PSD parameterization is greatly needed. Since a robust parameterization is based on good statistics on a variety of clouds, future field campaigns (from in situ as well as ground-based techniques) should focus more on this data-sparse region.

5. Conclusions and Future Work

[61] In this study we have described and validated MLS V2.2 IWC retrievals at 215−83 hPa through model simulations and comparisons with CloudSat data. The MLS V2.2 IWC data are scientifically useful at pressures between 261 and 83 hPa but the user needs to screen the data using the method described in section 2.5. The V2.2 IWC precision, accuracy, and resolution are assessed, and the results are summarized in Table 4.

[62] The V2.2 IWC measurements represent a spatially averaged quantity of which the volume size can be approximated with a rectangular box (∼4 km high and ∼300 km long along track) as shown in Figure 4. Roughly speaking, the dimensions of these rectangular boxes represent the vertical and horizontal (along-track) resolutions of the V2.2 IWC measurements, which are given in Table 4. The V2.2

IWC measurements generally have better precision at low pressures and at high latitudes than in other regions. Cloud inhomogeneity and PSD assumption contribute mostly to the uncertainties of the V2.2 IWC retrieval. Most of the inhomogeneity-induced uncertainties can be reduced through averaging (e.g., in monthly maps) because of randomness of the inhomogeneity. However, inhomogeneity-induced scaling errors in the V2.2 IWC retrieval, ranging from −70% to +80%, cannot be reduced by averaging. The inhomogeneity-induced uncertainty is larger at higher pressures and for smaller IWC values. Although our validation was focused on the measurements with IWC < 50 mg/m^3 where the *Tcir*-IWC relations are nearly linear, the data with values > 50 mg/m^3 are still qualitatively useful.

[63] The V2.2 algorithm is based on the simple *Tcir*-IWC relations derived from the 1-D geometry and prone to uncertainties induced by cloud inhomogeneity. Most of these uncertainties can be reduced substantially with a 2-D tomographic retrieval that is currently being developed by the MLS team. In addition to the retrievals using the 190−240 GHz radiances, a retrieval based on the 640 GHz measurements is also being investigated. At the higher frequencies, MLS *Tcir* has better sensitivity to cloud scattering from small ice crystals, and therefore increases ability of measuring cloud ice from tenuous cirrus [*Wu et al.*, 2006]. More importantly, the joint IWC retrievals from 240 and 640 GHz can provide bulk information on particle sizes of upper tropospheric ice clouds.

Appendix A: MLS V2.2 Level 2 Processing

[64] Like MLS V1.5 algorithm [*Livesey et al.*, 2006], the V2.2 software processes MLS radiance measurements through multiple phases. The cloud detection and the retrieved atmospheric state are improved together as the retrieval progresses in phase.

[65] Figure A1 illustrates the V2.2 data processing flow where cloud flags are updated several times as the retrieval progresses through its phases. The V2.2 cloud flags are based on *Tcir* estimated at the end of the earlier phase for R1, R2 and R4. Different fundamentally from V1.5 in R3 cloud detection, the V2.2 algorithm detects clouds on the basis of the χ^2 of the fitted radiance residuals near the 233.9 GHz $^{16}O^{18}O$ line (Band 8). The modeled clear-sky radiances are updated at the end of each retrieval phase from
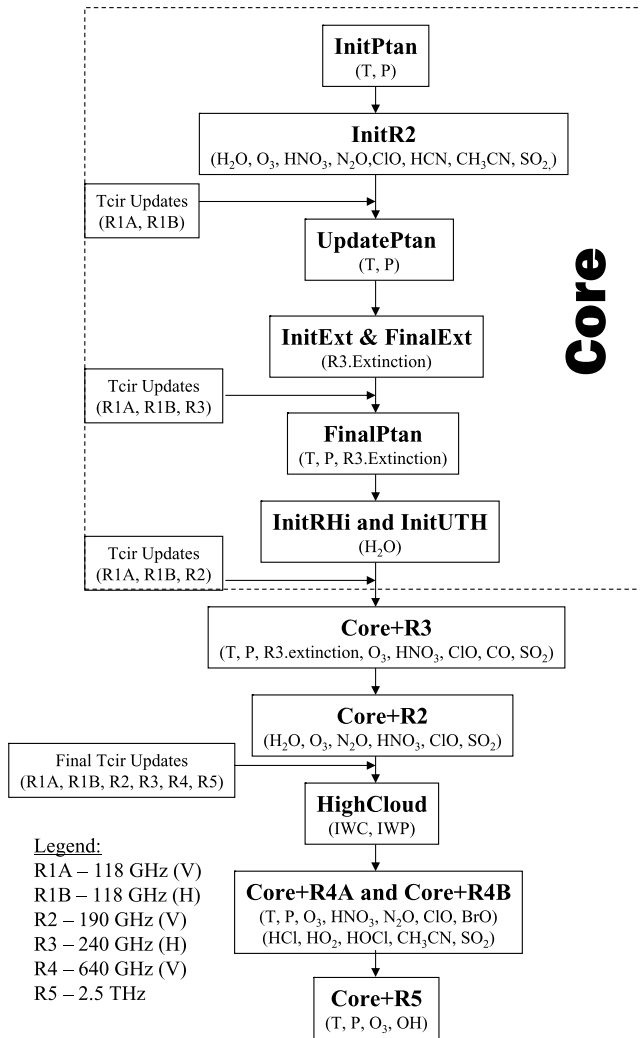
Figure A1. Data flow diagram of MLS V2.2 Level 2 processing. The atmospheric variables retrieved in each phase are listed in the parentheses. *Tcir* is updated three times in the *Core* phase to ensure stable retrievals of clear-sky gaseous species. MLS radiometers and their associated frequencies are given in the legend.

the newly retrieved atmospheric state. Atmospheric variables most important for determining *Tcir* are temperature (T), tangent pressure (*Ptan*), H_2O, O_3, HNO_3 profiles.

[66] As shown in Figure A1, the V2.2 retrieval phases contain *Core* (*InitPtan, InitR2, UpdatePtan, InitExt, FinalExt, FinalPtan, InitRHi* and *InitUTH*), *Core+R3*, *Core+R2*, *HighCloud*, *Core+R4* (A and B), and *Core+R5*. The *Core* phase is aimed to obtain a reliable initial atmospheric state through several subphases. The first two subphases, *InitPtan* and *InitR2*, are structured to obtain an initial estimate of atmospheric variables in the stratosphere, which use only radiances above cloud altitudes to avoid potential impacts from clouds. At the end these phases *Tcir*'s are estimated for the R1 radiances using the retrieved T, *Ptan* and other a priori profiles extended into the troposphere. The R1 radiances exceeding the cloud thresholds in Table A1 are flagged, and the flagged radiances are excluded in *UpdatePtan*, a subsequent phase

to retrieve T and *Ptan* once again by including the R1 radiances at the tropospheric tangent heights.

[67] The rest of the subphases in *Core* are configured to refine T and *Ptan* retrievals with a better vertical resolution and include the R2 radiances to obtain a good initial guess for the H_2O in the UT/LS region. Before using the R3 radiances, the V2.2 algorithm first retrieves a background total extinction profile using the window channel at 240 GHz, which accounts for most of the spectrally flat component in the R3 radiances. This retrieval is divided to two subphases, *InitExt* and *FinalExt*, to deal with potential cloud effects. The *InitExt* phase uses R3 window-channel radiances only at *Ptan* < 250 hPa so that the extinction retrieval is always converged in cloudy cases. The *FinalExt* phase is designed to further update the extinction profile retrieved in *InitExt* by using all the window-channel and Band 8 radiances down to the surface. However, the update may not occur in a bad cloudy case, and the extinction retrieval from *FinalExt* will relax to the *InitExt* profile if this happens. Large (>30) Band-8 χ^2 from *FinalExt* are used to flag R3 radiances on a MIF-by-MIF basis. The flagged R3 radiances are excluded in the *FinalPtan* phase that is configured to finalize T and *Ptan* retrievals using both R1 and R3 radiances.

[68] After the T and *Ptan* retrievals are completed, the last two subphases in *Core* are introduced to provide an initial guess for H_2O in the UT/LS region using R2 radiances, with *InitRHi* featuring the midtropospheric *RHi* and *InitUTH* featuring the UT/LS H_2O. No cloud flags are imposed for these retrievals, and the configured algorithms rely on their own skills to handle cloud impacts. For example, the *RHi* from *InitRHi* is capped at 110%; whereas *InitUTH* uses only R2 radiances at *Ptan* < 350 hPa and retrieves radiance baselines along with H_2O profile. Improved from V1.5, such a configuration performs well in dealing with cloudy cases and yields a reasonably good initial guess for the final H_2O retrieval in the next phase. Using the initial guess of H_2O, R1 and R2 *Tcir*'s are calculated at the end of *Core*.

[69] The phases after *Core* are essentially parallel to each other. Flagged radiances are excluded in *Core+R3* and *Core+R2* retrievals. The cloud ice retrieval, *HighCloud*, is placed after *Core+R3* and *Core+R2*, because the best *Tcir* estimate comes after T, *Ptan*, H_2O, O_3, and HNO_3 retrievals are finalized. The final *Tcir*'s for all radiometers are obtained in the *HighCloud* phase and averaged into the standard vertical pressure levels (12 levels per decade), which go to the cloud IWC and IWP retrievals. Additional frequency averaging is applied to R4 *Tcir* to further reduce radiance measurement noise. Neither *Core+R4* nor *Core+R5* uses the cloud flags for radiance discrimination.

Table A1. MLS Frequency Channels and Thresholds for Cloud Flag

Radiometer	Cloud Channel Frequency, GHz	Low Threshold	High Threshold
R1A/R1B, 118 GHz	B32.C4/B34.C4, 115.3	$Tcir < -4$ K	none
R2, 190 GHz	B5.C1, 178.8 and 204.9	$Tcir < -20$ K	$Tcir > 10$ K
R3, 240 GHz	B8, 233.4−234.5 and 244.8−245.9	none	$\chi^2 > 30$
R4, 640 GHz	B11.C23, 635.9 and 649.8	$Tcir < -10$ K	$Tcir > 10$ K

Appendix B: Cloud Profiles and Equivalent Limb Length for Average IWC

B1. Layered Clouds

[70] In the RT calculations with a 2-km layered cloud, we specify the cloud with a trapezoid profile with, i.e.,

$$w(z - z_c) = \begin{cases} 0 & z - z_c > 1 \\ 2(1 - z + z_c) & 1 > z - z_c > 0.5 \\ 1 & 0.5 > z - z_c > -0.5 \\ 2(1 + z - z_c) & -0.5 > z - z_c > -1 \\ 0 & z - z_c < -0.5. \end{cases}$$

where z_c is the center of the cloud layer, and $IWC(z) = IWC_0 \bullet w(z-z_c)$. Hence, at tangent height $h_t = z_c$, we have

$$hIWP = 2 \int_{z_c}^{\infty} IWC(z)ds = 2IWC_0 \int_{z_c}^{\infty} w(z)ds = IWC_0 \bullet L$$

where $L = 192$ km is the equivalent path length for a cloud with average IWC_0. As a result, for the limb radiance at $h_t = z_c$, if $hIWP$ is small, $Tcir$ is proportional to $hIWP$ and to the averaged IWC of the cloud layer with an equivalent path length of ~200 km.

B2. Clouds With Exponentially Decreasing IWC

[71] In the case where $IWC \propto e^{-z/H_0}$, we have

$$hIWP = 2IWC_0 \int_{h_t}^{\infty} e^{-z/H_0} ds$$
$$= 2IWC_0 \int_{h_t}^{\infty} e^{-z/H_0} \frac{R_e + z}{\sqrt{(R_e + z)^2 - (R_e + h_t)^2}} dz$$
$$\approx 2IWC_0 e^{-h_t/H_0} \int_0^{\infty} e^{-z/H_0} \frac{R_e}{\sqrt{2R_e z}} dz$$
$$\approx IWC(h_t) \sqrt{2R_e H_0} \Gamma(0.5)$$

where R_e is the Earth's radius in km, H_0 is the scale height of decreasing IWC profile in km, and Gamma function $\Gamma(0.5)$ is 1.77. For small $hIWP$, we still obtain a relation that $Tcir$ is proportional to IWC at the pointing tangent height. In this case, the equivalent path length $l = \sqrt{2R_e H_0} \Gamma(0.5) \approx 200\sqrt{H_0}$ in km. As suggested by the observed IWC climatology in the upper troposphere, H_0 varies typically between 1 and 2 km. For $H_0 = 1$ km, $L = $ ~200 km; for $H_0 = 2$ km, $L = $ ~280 km.

[72] The distribution $IWC \propto e^{-z/H_0}$ also shifts contribution functions to a low altitude if the limb radiance has a finite beam width. MLS 240-GHz receiver has a Gaussian beam pattern with 3.2 km half-power beam width (HPBW), i.e., $e^{-(z-h_t)^2/2w^2}$, where $w = 0.425 \bullet HPBW$. Unlike the WFs in Figure 4, which are centered at tangent height h_t, the contribution after convolving with $IWC \propto e^{-z/H_0}$ will shift down by w^2/H_0. If HPBW = 3.2 km, the shift will be 1.8 km for $H_0 = 1$ km and 0.9 km for $H_0 = 2$ km. In other words, we need to increase the width of vertical resolution from 3.2 km to 5 km for $H_0 = 1$ km and 4.1 km for $H_0 = 2$ km to embrace most of the contribution from profiles like $IWC \propto e^{-z/H_0}$.

References

Austin, R. T., and G. L. Stephens (2001), Retrieval of stratus cloud microphysical parameters using millimeter-wave radar and visible optical depth in preparation for CloudSat: 1. Algorithm formulation, *J. Geophys. Res.*, *106*, 28,233–28,242, doi:10.1029/2000JD000293.

Benedetti, A., G. L. Stephens, and J. M. Haynes (2003), Ice cloud microphysics retrievals from millimeter radar and visible optical depth using an estimation theory approach, *J. Geophys. Res.*, *108*(D11), 4335, doi:10.1029/2002JD002693.

Brown, P. R. A., and P. N. Francis (1995), Improved measurements of the ice water content in cirrus using a total-water probe, *J. Atmos. Oceanic Technol.*, *12*, 410–414, doi:10.1175/1520-0426(1995)012<0410:IMOTIW>2.0.CO;2.

Cofield, R. E., and P. C. Stek (2006), Design and field-of-view calibration of 114–660 GHz optics of the Earth Observing System Microwave Limb Sounder, *IEEE Trans. Geosci. Remote Sens.*, *44*(5), 1166–1181, doi:10.1109/TGRS.2006.873234.

Comstock, J. M., et al. (2007), An intercomparison of microphysical retrieval algorithms for upper-tropospheric ice clouds, *Bull. Am. Meteorol. Soc.*, *88*, 191–204, doi:10.1175/BAMS-88-2-191.

Davis, C. P., C. Emde, and R. S. Harwood (2005a), A 3D polarized reversed Monte Carlo radiative transfer model for mm and sub-mm passive remote sensing in cloudy atmospheres, *IEEE Trans. Geosci. Remote Sens.*, *43*(5), 1096–1101.

Davis, C. P., D. L. Wu, C. Emde, J. H. Jiang, R. E. Cofield, and R. S. Harwood (2005b), Cirrus induced polarization in 122 GHz Aura Microwave Limb Sounder radiances, *Geophys. Res. Lett.*, *32*, L14806, doi:10.1029/2005GL022681.

Davis, C. P., H. C. Pumphrey, K. F. Evans, S. Buehler, and D. L. Wu (2007), 3D polarised simulations of space-borne passive mm/sub-mm midlatitude cirrus observations: A case study, *Atmos. Chem. Phys.*, *7*, 4149–4158.

Delanoë, J., et al. (2005), Statistical properties of the normalized ice particle size distribution, *J. Geophys. Res.*, *110*, D10201, doi:10.1029/2004JD005405.

Donovan, D. P., and C. A. P. A.van Lammeren (2002), First ice cloud effective particle size parameterization based on combined lidar and radar data, *Geophys. Res. Lett.*, *29*(1), 1006, doi:10.1029/2001GL013731.

Eriksson, P., M. Ekström, B. Rydberg, and D. P. Murtagh (2007), First Odin sub-mm retrievals in the tropical upper troposphere: ice cloud properties, *Atmos. Chem. Phys.*, *7*, 471–482.

Evans, K. F., and G. L. Stephens (1995), Microwave radiative transfer through clouds composed of realistically shaped ice crystals. Part II: Remote sensing of ice clouds, *J. Atmos. Sci.*, *52*, 2058–2072, doi:10.1175/1520-0469(1995)052<2058:MRTTCC>2.0.CO;2.

Evans, K. F., et al. (1998), Modeling of submillimeter passive remote sensing of cirrus clouds, *J. Appl. Meteorol.*, *37*, 184–205, doi:10.1175/1520-0450(1998)037<0184:MOSPRS>2.0.CO;2.

Evans, K. F., J. R. Wang, P. E. Racette, G. M. Heymsfield, and L. Li (2005), Ice cloud retrievals and analysis with the compact scanning submillimeter imaging radiometer and the cloud radar system during CRYSTAL FACE, *J. Appl. Meteorol.*, *44*, 839–859, doi:10.1175/JAM2250.1.

Field, P. R., et al. (2005), Parametrization of ice-particle size distributions for mid-latitude stratiform cloud, *Q.J.R. Meteorol. Soc.*, *131*, 1997–2017.

Fleming, E. L., S. Chandra, M. R. Schoeberl, and J. J. Barnett (1988). Monthly mean global climatology of temperature, wind, geopotential height and pressure for 0–120 km, *NASA Tech. Memo., 100697*.

Fu, R., et al. (2006), Short circuit of water vapor and polluted air to the global stratosphere by convective transport over the Tibetan Plateau, *Proc. Natl. Acad. Sci. U.S.A.*, *103*(15), 5664–5669.

Gasiewski, A. J. (1992), Numerical sensitivity analysis of passive EHF and SMMW channels to tropospheric water vapor, clouds, and precipitation, *IEEE Trans. Geosci. Remote Sens.*, *30*(5), 859–870.

Geerts, B., G. M. Heymsfield, L. Tian, J. B. Halverson, A. Guillory, and M. I. Mejia (2000), Hurricane Georges's landfall in the Dominican Republic: Detailed airborne Doppler radar imagery, *Bull. Am. Meteorol. Soc.*, *81*, 999–1018, doi:10.1175/1520-0477(2000)081<0999:HGLITD>2.3.CO;2.

Heymsfield, A. J., and L. J. Donner (1990), A scheme for parameterizing ice-cloud water in general circulation models, *J. Atmos. Sci.*, *47*, 1865–1877, doi:10.1175/1520-0469(1990)047<1865:ASFPIC>2.0.CO;2.

Heymsfield, A. J., A. Bansemer, P. R. Field, S. L. Durden, J. L. Stith, J. E. Dye, W. Hall, and C. A. Grainger (2002), Observations and parameter-

izations of particle size distributions in deep tropical cirrus and stratiform precipitating clouds: Results from in situ observations in TRMM field campaigns, *J. Atmos. Sci.*, 59, 3457–3491, doi:10.1175/1520-0469(2002)059<3457:OAPOPS>2.0.CO;2.

Hogan, R. J., and A. J. Illingworth (2003), Parameterizing ice cloud inhomogeneity and the overlap of inhomogeneities using cloud radar data, *J. Atmos. Sci.*, 60, 756–767, doi:10.1175/1520-0469(2003)060<0756:PICIAT>2.0.CO;2.

Hogan, R. J., A. J. Illingworth, and J. P. V. Poilares Baptista (2003), Characteristics of mixed-phase clouds. Part II: A climatology from ground-based lidar, *Q.J.R. Meteorol. Soc.*, 129, 2117–2134, doi:10.1256/qj.01.209.

Houghton, J. T., et al. (2001). Climate Change 2001: The Scientific Basis, 944 pp., Cambridge Univ. Press, New York.

Jarnot, R. F., V. S. Perun, and M. J. Schwartz (2006), Radiometric and spectral performance and calibration of the GHz bands of EOS MLS, *IEEE Trans. Geosci. Remote Sens.*, 44(5), 1131–1143, doi:10.1109/TGRS.2005.863714.

Jiang, Y. B., et al. (2007), Validation of the Aura Microwave Limb Sounder ozone by ozonesonde and lidar measurements, *J. Geophys. Res.*, 112, D24S34, doi:10.1029/2007JD008776.

Korolev, A. V., G. A. Isaac, I. P. Mazin, and H. W. Barker (2001), Microphysical properties of continental clouds from in situ measurements, *Q.J.R. Meteorol. Soc.*, 127, 2117–2151.

Lary, D. J., and L. Lait (2006), Using probability distribution functions for satellite validation, *IEEE Trans. Geosci. Remote Sens.*, 44(5), 1359–1366, doi:10.1109/TGRS.2005.860662.

Li, J.-L., et al. (2005), Comparisons of EOS MLS cloud ice measurements with ECMWF analyses and GCM simulations: Initial results, *Geophys. Res. Lett.*, 32, L18710, doi:10.1029/2005GL023788.

Li, J.-L., J. H. Jiang, D. E. Waliser, and A. M. Tompkins (2007), Assessing consistency between EOS MLS and ECMWF analyzed and forecast estimates of cloud ice, *Geophys. Res. Lett.*, 34, L08701, doi:10.1029/2006GL029022.

Li, Q. B., et al. (2005), Convective outflow of South Asian pollution: A global CTM simulation compared with EOS MLS observations, *Geophys. Res. Lett.*, 32, L14826, doi:10.1029/2005GL022762.

Liu, G., and J. A. Curry (2000), Determination of ice water path and mass median particle size using multichannel microwave measurements, *J. Appl. Meteorol.*, 39, 1318–1329, doi:10.1175/1520-0450(2000)039<1318:DOIWPA>2.0.CO;2.

Livesey, N. J., W. V. Snyder, W. G. Read, and P. A. Wagner (2006), Retrieval algorithms for the EOS Microwave Limb Sounder (MLS) instrument, *IEEE Trans. Geosci. Remote Sens.*, 44(5), 1144–1155, doi:10.1109/TGRS.2006.872327.

Livesey, N. J., et al. (2008), Validation of Aura Microwave Limb Sounder O_3 and CO observations in the upper troposphere and lower stratosphere, *J. Geophys. Res.*, 113, D15S02, doi:10.1029/2007JD008805.

Mace, G. G., E. E. Clouthiaux, and T. P. Ackerman (2001), The composite characteristics of cirrus clouds: Bulk properties revealed by one year of continuous cloud radar data, *J. Clim.*, 14, 2185–2203, doi:10.1175/1520-0442(2001)014<2185:TCCOCC>2.0.CO;2.

McFarquhar, G. M., and A. J. Heymsfield (1996), Microphysical characteristics of three anvils sampled during the central equatorial pacific experiment, *J. Atmos. Sci.*, 53, 2401–2423, doi:10.1175/1520-0469(1996)053<2401:MCOTAS>2.0.CO;2.

McFarquhar, G. M., and A. J. Heymsfield (1997), Parameterization of tropical cirrus ice crystal size distributions and implications for radiative transfer: Results from CEPEX, *J. Atmos. Sci.*, 54, 2187–2200, doi:10.1175/15200469(1997)054<2187:POTCIC>2.0.CO;2.

Pickett, H. M. (2006), Microwave Limb Sounder THz module on Aura, *IEEE Trans. Geosci. Remote Sens.*, 44(5), 1122–1130, doi:10.1109/TGRS.2005.862667.

Platt, C. M. R. (1997), A parameterization of the visible extinction coefficient in terms of the ice/water content, *J. Atmos. Sci.*, 48, 2083–2098, doi:10.1175/1520-0469(1997)054<2083:APOTVE>2.0.CO;2.

Read, W. G., Z. Shippony, M. J. Schwartz, N. J. Livesey, and W. V. Snyder (2006), The clear-sky unpolarized forward model for the EOS Microwave Limb Sounder (MLS), *IEEE Trans. Geosci. Remote Sens.*, 44(5), 1367–1379, doi:10.1109/TGRS.2006.873233.

Read, W. G., et al. (2007), Aura Microwave Limb Sounder upper tropospheric and lower stratospheric H2O and relative humidity with respect to ice validation, *J. Geophys. Res.*, 112, D24S35, doi:10.1029/2007JD008752.

Santee, M. L., et al. (2007), Validation of the Aura Microwave Limb Sounder HNO3 measurements, *J. Geophys. Res.*, 112, D24S40, doi:10.1029/2007JD008721.

Schwartz, M. J., et al. (2008), Validation of the Aura Microwave Limb Sounder temperature and geopotential height measurements, *J. Geophys. Res.*, doi:10.1029/2007JD008783, in press.

Skofronick-Jackson, G. M., and J. R. Wang (2000), The estimation of hydrometeor profiles from wideband microwave observations, *J. Appl. Meteorol.*, 39, 1645–1656.

Stephens, G. L., et al. (2002), The CloudSat mission and the EOS constellation: A new dimension of space-based observations of clouds and precipitation, *Bull. Am. Meteor. Soc.*, 83, 1771–1790, doi:10.1175/BAMS-83-12-1771.

Su, H., W. G. Read, J. H. Jiang, J. W. Waters, D. L. Wu, and E. J. Fetzer (2006), Enhanced positive water vapor feedback associated with tropical deep convection: New evidence from Aura MLS, *Geophys. Res. Lett.*, 33, L05709, doi:10.1029/2005GL025505.

van Zadelhoff, G.-J., D. P. Donovan, H. Klein Baltink, and R. Boers (2004), Comparing ice cloud microphysical properties using CloudNET and Atmospheric Radiation Measurement Program data, *J. Geophys. Res.*, 109, D24214, doi:10.1029/2004JD004967.

Vivekanandan, J., J. Turk, and V. N. Bringi (1991), Ice water path estimation and characterization using passive microwave radiometry, *J. Appl. Meteorol.*, 30, 1407–1421, doi:10.1175/1520-0450(1991)030<1407:IWPEAC>2.0.CO;2.

Waters, J. W. (1993). Microwave limb sounding, in *Atmospheric Remote Sensing by Microwave Radiometry*, edited by M. A. Janssen, pp. 383–496, John Wiley, Hoboken, N.J.

Waters, J. W., et al. (2006), The Earth Observing System Microwave Limb Sounder (EOS MLS) on the Aura satellite, *IEEE Trans. Geosci. Remote Sens.*, 44(5), 1075–1092, doi:10.1109/TGRS.2006.873771.

Weng, F., and N. C. Grody (2000), Retrieval of ice cloud parameters using a microwave imaging radiometer, *J. Atmos. Sci.*, 57, 1069–1081, doi:10.1175/1520-0469(2000)057<1069:ROICPU>2.0.CO;2.

Wilheit, T. T., et al. (1982), Microwave radiometric observations near 19.35, 95 and 183 GHz of precipitation in tropical storm Cora, *J. Appl. Meteorol.*, 21, 1137–1145, doi:10.1175/1520-0450(1982)021<1137:MRONAG>2.0.CO;2.

Wu, D. L. and J. H. Jiang (2004). EOS MLS algorithm theoretical basis for cloud measurements, *JPL Doc. 19299*, Jet Propul. Lab., Pasadena, Calif.

Wu, D. L., W. G. Read, A. E. Dessler, S. C. Sherwood, and J. H. Jiang (2005), UARS MLS cloud ice measurements and implications for H2O transport near the tropopause, *J. Atmos. Sci.*, 62(2), 518–530, doi:10.1175/JAS-3382.1.

Wu, D. L., J. H. Jiang, and C. P. Davis (2006), EOS MLS cloud ice measurements and cloudy-sky radiative transfer model, *IEEE Trans. Geosci. Remote Sens.*, 44(5), 1156–1165, doi:10.1109/TGRS.2006.869994.

Yeh, H.-Y. M., N. Prasad, R. A. Mack, and R. F. Adler (1990), Aircraft microwave observation and simulations of deep convection from 8 to 183 GHz, part I: Model results, *J. Atmos. Oceanic Technol.*, 7, 392–410, doi:10.1175/1520-0426(1990)007<0392:AMOASO>2.0.CO;2.

––––––––––––––

R. T. Austin and G. L. Stephens, Department of Atmospheric Science, Colorado State University, Fort Collins, CO 80523, USA.

C. P. Davis, Meteorological Service of New Zealand Limited, P.O. Box 722, Wellington 6140, New Zealand.

J. H. Jiang, A. Lambert, W. G. Read, D. G. Vane, J. W. Waters, and D. L. Wu, Jet Propulsion Laboratory, California Institute of Technology, Pasadena, CA 91109, USA. (dwu@mls.jpl.nasa.gov)